

Three-Axis Flexible Spacecraft Attitude Control with Disturbance Observer-Based PD Control

5. Three-Axis Flexible Spacecraft Attitude Control with Disturbance Observer-Based PD Control

5.1. Introduction:

In this chapter, we will discuss the primary control strategies for stabilizing the three-axis attitude of a flexible spacecraft using quaternion representations to ensure accurate dynamic modeling. The focus will be on proportional-derivative (PD) control, which is widely used due to its simplicity and ease of implementation. However, PD control has limitations when dealing with significant disturbances and model uncertainties, which are crucial factors in the space environment.

To improve the control system's robustness, we will implement a disturbance observer-based control (DOBC) approach. This method estimates and compensates for external disturbances, enhancing the overall stability and performance of the spacecraft. Additionally, we will utilize Particle Swarm Optimization (PSO) to fine-tune the parameters of the PD and DOBC controllers. PSO is an efficient optimization algorithm inspired by the social behavior of birds flocking. It ensures optimal controller performance by finding the best parameter values, thus addressing the complex dynamic challenges associated with flexible spacecraft attitude control.

5.2. Problem statement

Given any initial attitude and angular velocity, the control objective is to design a controller for the system such that $\lim_{t \rightarrow \infty} q_{ve} = 0$ and $\lim_{t \rightarrow \infty} \omega_e = 0$, where ω_e is the error of attitude angular velocity.

Since the system is affected by disturbances, it is necessary to estimate them. This information can be obtained by designing a dynamic system for disturbance observation, which provides an approximation of d as outputs [48].

Based on the considerations mentioned above and the need to control flexible satellites affected by bending and vibration, this study introduces a composite control method for attitude control and stabilization (DOBC-PD). Firstly, the attitude kinematic equation is formulated using error quaternions. Then, a dynamic PD control law for flexible spacecraft attitude control is developed. Following this, a disturbance observer is designed to estimate the vibration caused by the solar panels, which is considered as an internal disturbance. An optimization technique called Particle Swarm Optimization (PSO) is employed to adjust the gains of the controller and observer automatically. This method offers a significant advantage over previous approaches, as it eliminates the need for manual tuning, which is typically a time-consuming and iterative process. Finally, simulation results demonstrate that the proposed composite control dynamic can effectively achieve attitude control of a flexible spacecraft.

5.2.1. Kinematics Equation

The unit quaternion is used to describe the kinematics equation for global rotation representation without singularity. The attitude kinematics of a spacecraft can be modeled as (see [49, 50])

$$\begin{aligned}\dot{q} &= \frac{1}{2}(q^{\times} + q_4 I_3)\omega \\ \dot{q}_4 &= \frac{1}{2}q^T \omega\end{aligned}\tag{5.1}$$

5.2.2. Flexible Spacecraft Dynamics

The dynamic equations of a spacecraft with flexible appendages can be expressed by taking the assumption of small elastic deformations.

$$\begin{aligned}J\dot{\omega} + \omega^{\times}(J\omega + \delta\dot{\eta}) + \delta\ddot{\eta} &= u + d_1 \\ \ddot{\eta} + C\dot{\eta} + K\eta + \delta^T\dot{\omega} &= 0\end{aligned}\tag{5.2}$$

where $J \in R^{3 \times 3}$ is the total inertia matrix of the spacecraft, $\omega \in R^{3 \times 3}$ is the angular velocity of the spacecraft in the body frame, $u \in R^3$ is the control torque input vector, $d_1 \in R^3$ is the external disturbance torque vector, and η is the modal coordinate vector of the flexible appendage, δ is the coupling matrix between the flexible appendage and the rigid dynamics, $K = \text{diag}(\Lambda_i^2)$ denotes the stiffness matrix with i being the number of flexible modes considered, $C = \text{diag}(2\xi_i\Lambda_i)$ represents the damping matrix with Λ the natural frequencies, and ξ the associated damping.

The terms d_1 , $\delta\ddot{\eta}$ and $\omega^{\times}\delta\dot{\eta}$ are considered the lumped disturbances for the rigid dynamics, eq. (5.2) can be rewritten as :

$$J\dot{\omega} = -\omega^{\times}J\omega + u + d\tag{5.3}$$

where $d = d_1 + d_0$ and the item $d_0 = -\delta\ddot{\eta} - \omega^{\times}\delta\dot{\eta}$ is considered as the disturbance due to elastic vibration of the flexible appendages.

5.3. PD Controller Design

The proportional gain controls the system's response to the error between the desired attitude and the satellite's actual attitude. In contrast, the derivative gain controls the system's response to the rate of change of the error. By adjusting these two gains, the control system can respond quickly to changes in attitude while minimizing overshoot and oscillation.

An advantage of PD control is its ease of implementation and tuning in spacecraft attitude control. The derivative gain controls the system's response to the rate of change of the error. In contrast, the proportional gain controls the system's response to the difference between the spacecraft's actual and desired attitudes. By adjusting these two gains, the control system can minimize overshoot and oscillations while responding quickly to attitude changes.

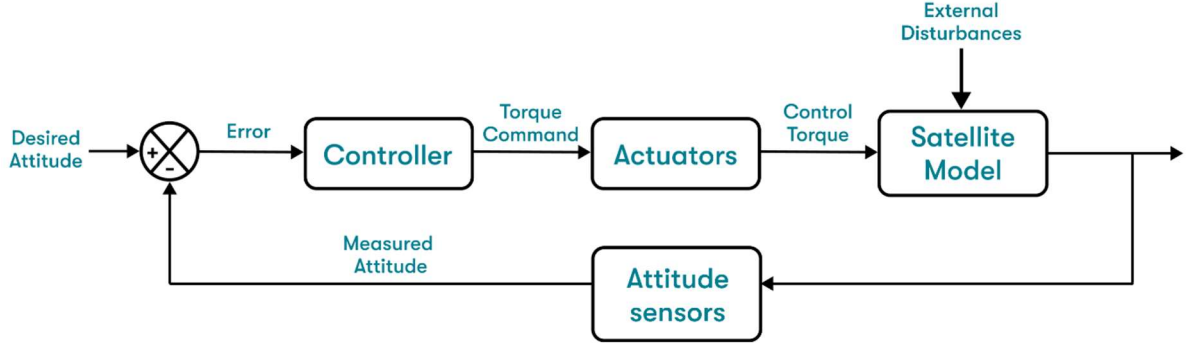


Fig 5.1: Block schematic of spacecraft attitude control systems.

Using the quaternion representation in Eq (2.14), the control law is:

$$\begin{aligned}
 u_x &= K_x q_{e1} + K_{dx} \omega_x \\
 u_y &= K_y q_{e2} + K_{dy} \omega_y \\
 u_z &= K_z q_{e3} + K_{dz} \omega_z
 \end{aligned} \tag{5.4}$$

where K_x, K_y, K_z are the proportional gains, while K_{dx}, K_{dy} and K_{dz} are the derivative gains. ω_x, ω_y and ω_z are then angular velocities and q_{e1}, q_{e2} and q_{e3} are computed from chapter2 Eq(2.14). Let us consider the control law expressed in equation (4). This equation can be rewritten as follows:

$$u = -K_p q - K_d \omega$$

Driving along system trajectories, the following Lyapunov function candidate:

$$V = K_p \left[(q_0 - 1)^2 + q^T q \right] + \left(\frac{1}{2} \right) \omega^T J \omega$$

with $K_p > 0$, one obtains

$$\dot{V} = K_p q^T \omega + \omega^T (-\omega \times J \omega + u) = -K_d \omega^T \omega \leq 0$$

Since V is a continuously differentiable and positive definite function with a negative semi-definite time derivative over the entire state space, the global asymptotic stability [51,52].

The following section presents the strategy for attitude control based on disturbance observer. As mentioned earlier, a disturbance observer, along with PD control, is designed to eliminate all disturbances acting on the model and achieve the desired attitude.

5.4. Disturbance Observer design

The block diagram of the proposed disturbance observer is illustrated in Figure 1. As shown in the figure, the composite controller comprises two parts: a disturbance observer and a PD controller. First, the disturbance observer estimates the vibrations caused by the flexible appendages, which are then compensated for. Subsequently, the PD controller regulates the attitude of the spacecraft. [31]

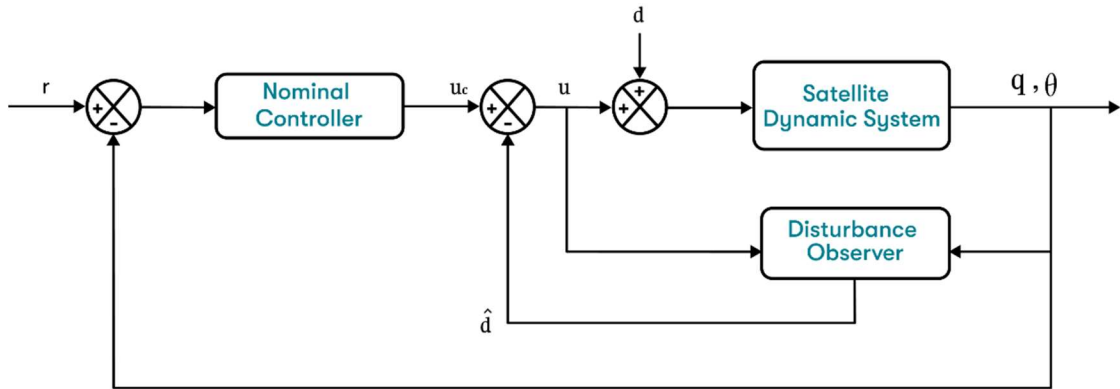


Fig 5.2: Block diagram of the ACS.

A general design procedure is proposed for the following disturbance observer-based control (DOBC) design:

- Step 1: Design a controller for the system to achieve stability and other desired performance specifications, assuming the disturbance is measurable.
- Step 2: Design a disturbance observer to estimate the disturbance signal.
- Step 3: Integrate the disturbance observer with the controller by replacing the actual disturbance in the control law with its estimated value from the disturbance observer.

According to system (5.3), we formulate the disturbance observer as

$$\begin{cases} \dot{z} = -L\hat{d} + L(\omega^\times J\omega - u) \\ \hat{d} = z + LJ\omega \end{cases} \quad (5.5)$$

Where z the internal variable vector of the observer, $L = \beta I_{3 \times 3}$ the observe gain to be designed and \hat{d} is the estimation of d . Using the estimation of disturbance \hat{d} , the controller can be constructed as

$$u = u_c - \hat{d} \quad (5.6)$$

$$u = -K_p q_e - K_d \omega_i - \hat{d} \quad (5.7)$$

Where u_c is designed by any control method to achieve stability

The error of disturbance observer is defined as

$$e = d - \hat{d} \quad (5.8)$$

According to the practical situation of the flexible spacecraft, we should design an appropriate L to make $e \rightarrow 0$. Therefore, the disturbance estimate \hat{d} can converge to d .

In order to achieve stability of the closed-loop system, the following assumption is needed

Assumption 1 The lumped disturbances d are slowly varying and have constant values in steady-state, i.e. $\lim_{t \rightarrow \infty} \dot{d} = 0$

Proof The error dynamics can be described for this disturbance observer by

$$\dot{e} = \dot{d} - \dot{\hat{d}} \quad (5.9)$$

Substitution of the derivative of \hat{d} in eq. (5.9) yields:

$$\dot{e} = \dot{d} - \dot{z} - LJ\dot{\omega} \quad (5.10)$$

Substituting eq. (5.3) and (5.5) into (5.10) we get:

$$\dot{e} = \dot{d} + L\hat{d} - L\omega^\times J\omega + Lu - L(-\omega^\times J\omega + d + u) \quad (5.11)$$

Then

$$\dot{e} = \dot{d} - Le \quad (5.12)$$

It can be verified that the disturbance estimation error of the DO is asymptotically stable since d is bounded and satisfies $\lim_{t \rightarrow \infty} \dot{d} = 0$. This implies that the disturbance estimate of DO can track the disturbances asymptotically with the designed controller.

5.5. Simulation and result analysis

To demonstrate the effectiveness of the proposed control schemes, numerical simulations using MATLAB/SIMULINK have been performed and are presented in this section to ensure that our objective is achieved.

Table 5.1: Spacecraft Model Parameters.

Parameters	Symbol	Value
Spacecraft inertia matrix [kg.m ²]	J	$\begin{bmatrix} 420.8 & 8.9 & 1.2 \\ 8.9 & 175.4 & 3.3 \\ 1.2 & 3.3 & 380.3 \end{bmatrix}$
Coupling matrix [kg ^{1/2} m/s ²]	δ	$\begin{bmatrix} 1 & 0.1 & 0.1 \\ -1 & 0.1 & 0.01 \\ -0.1 & 0.1 & 0.01 \end{bmatrix}$
Damping rate	ξ	$\begin{bmatrix} 0.05 & 0 & 0 \\ 0 & 0.05 & 0 \\ 0 & 0 & 0.05 \end{bmatrix}$
Natural frequencies [rad/s]	Λ	$\begin{bmatrix} 1.9015 & 0 & 0 \\ 0 & 2.7512 & 0 \\ 0 & 0 & 3.1224 \end{bmatrix}$
Spacecraft orbital velocity [rad/s]	ω_o	$[0 \quad \theta_{ref} \quad 0]^T$
Desired angular velocity [rad/s]	ω_d	$[0 \quad 0 \quad 0]^T$
Desired Euler angles [deg]	$[\phi_{ref} \quad \theta_{ref} \quad \psi_{ref}]^T$	$[0 \quad 0 \quad 0]^T$
Desired quaternions	q_{ref}	$[0 \quad 0 \quad 0 \quad 1]$
Initial Euler angles [deg]	$[\phi_0 \quad \theta_0 \quad \psi_0]^T$	$[10 \quad -20 \quad 25]^T$

This section presents a simulation to demonstrate the proposed attitude control technique's effectiveness for a rigid satellite with two symmetric solar arrays, verifying the controller's performance. The external disturbance torque is modeled as in [53] with

$$d_1 = 10^{-3} \begin{bmatrix} -3 + 3 \cos(0.01t) - 4.5 \sin(0.02t) + 3\omega_1 \cos(0.015t) \\ 6 + 4.5 \sin(0.01t) - 6 \cos(0.02t) - 6\omega_2 \sin(0.015t) \\ -6 + 6 \sin(0.01t) + 4.5 \cos(0.02t) - 3\omega_3 \sin(0.015t) \end{bmatrix} \text{ N/m} \quad (5.13)$$

The PD controller parameters are selected as follows [54]:

Table 5.1: The PD controller design parameters.

Controller part	Control gain	Value
DOBC	β	6.5
Proportional Matrix	K	$30 \times I_3$
Derivative Gain	D	$500 \times I_3$
Improved Proportional Matrix	K	$1000 \times I_3$
Improved Derivative Gain	D	$546.1 \times I_3$

To enhance the tuning speed and accuracy for the PD controller parameters, an Improved PD (IPD) controller is designed using a Particle Swarm Optimization (PSO) approach. For the PD-based PSO parameter optimization process, the particle swarm size is set to 50, the maximum number of iterations is 200, and the learning factors are set to 2. The convergence of the fitness function value during the optimization process is shown in Figure 3. From the simulation results, it can be observed that after approximately 18 iterations, the system control accuracy stabilizes at around 7.363×10^5 .

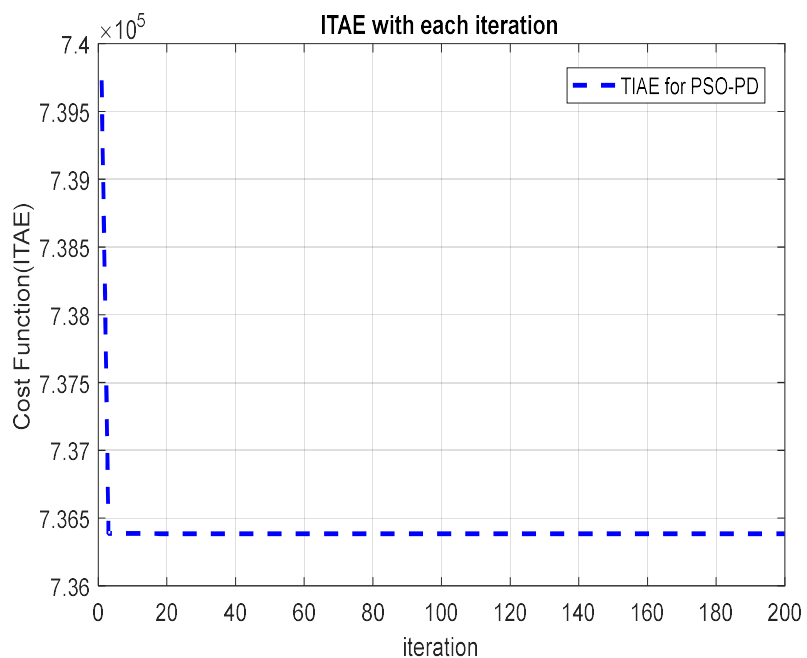


Fig 5.3: Fitness function curve.

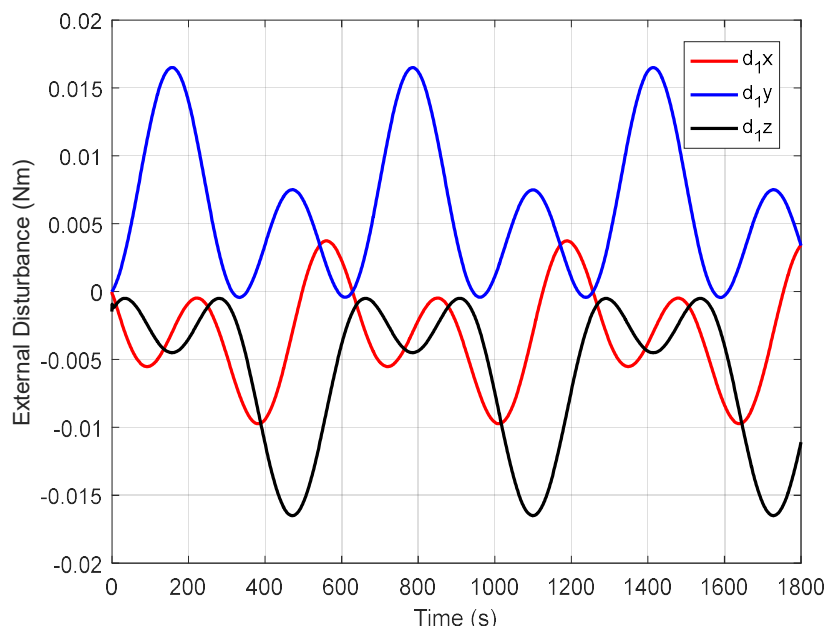


Fig 5.4: External Disturbances.

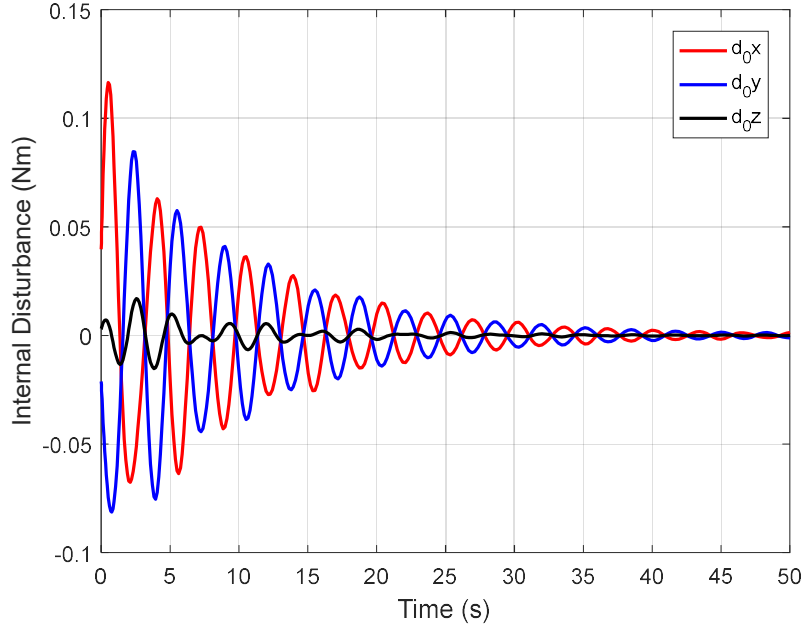


Fig 5.5: Internal Disturbances.

Fig 5.4 and 5.5 illustrate the time responses of the external and internal disturbance torques acting on the spacecraft. The external disturbances, denoted as d_1 , represent the space environment torques. The internal disturbances, denoted as d_0 , arise from the flexible appendages of the spacecraft. Upon examining these figures, it is evident that the external disturbances have relatively small magnitudes compared to the internal disturbances. The internal disturbances exhibit significantly larger magnitudes and more complex dynamical behavior, likely due to the spacecraft's structural flexibility and the coupling between the rigid-body and flexible modes.

5.5.1. Spacecraft model without the Disturbance Observer

As discussed in the previous chapters, spacecraft are subjected to various disturbances that can cause significant deviations in their attitude and angular velocity. To evaluate the performance enhancement achieved by tuning the PD controller parameters using the PSO method, a comparative study is conducted. This study compares the system response with randomly selected controller parameters against the response obtained using the optimized parameters from the PSO-based tuning process.

By using the flexible spacecraft parameters provided in Table 5.1, the simulation results are presented as follows:

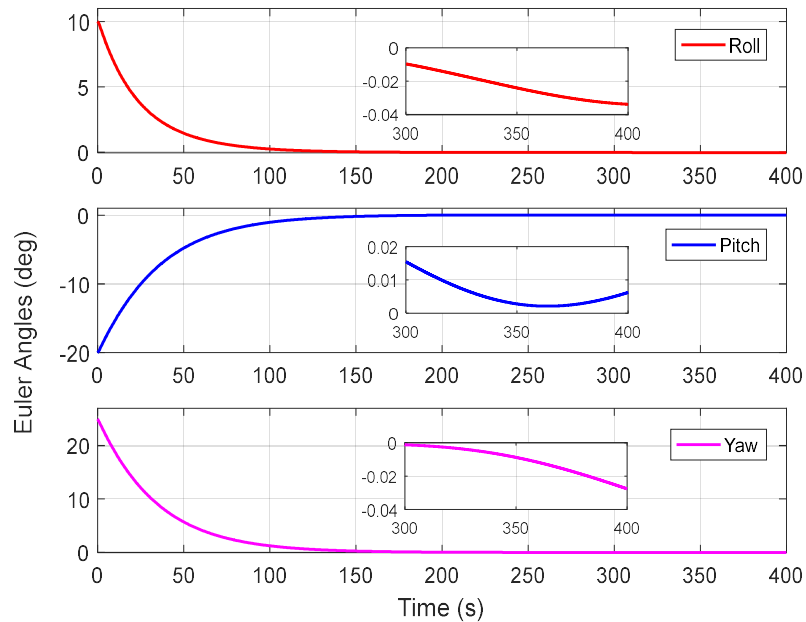


Fig 5.6: Euler Angles using only PD control.

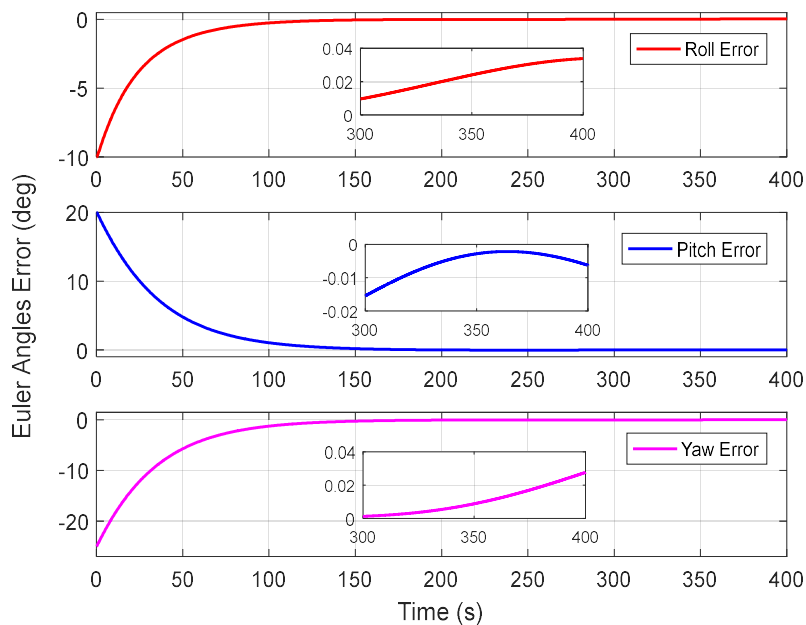


Fig 5.7: Euler angles error using only PD control.

Fig 5.6 and 5.7 illustrate the Euler angle responses and Euler angle tracking errors when adopting two different controllers, respectively. It can be observed that the system achieves the trajectory, and the Euler angles follow the reference trajectory with a noticeable delay. with a settling time of $\langle 112.2603 \ 129.46 \ 5130.717 \rangle$ s and errors under 4.5×10^{-2} .

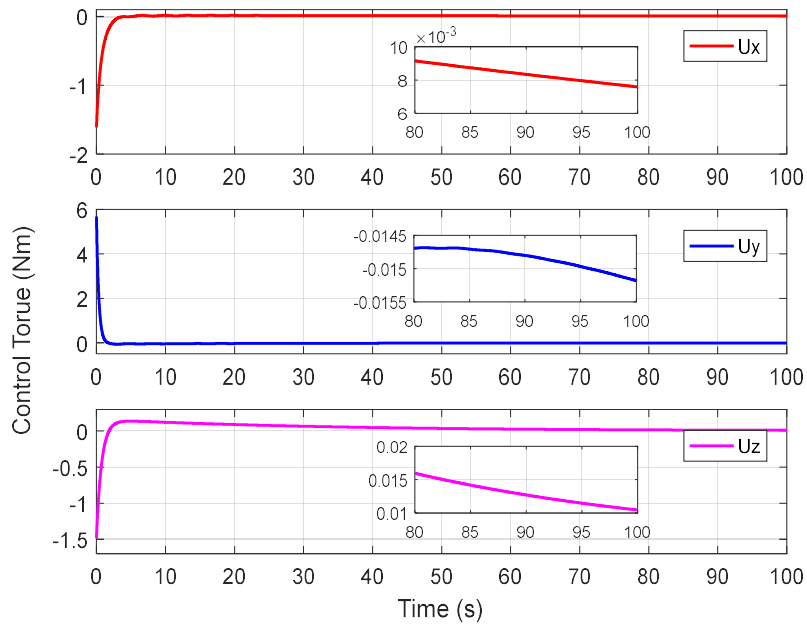


Fig 5.8: Control torque using only PD control.

Fig 5.8 represents the control torque acting on the system, where we observed that the torque aligns with the desired reference control value.

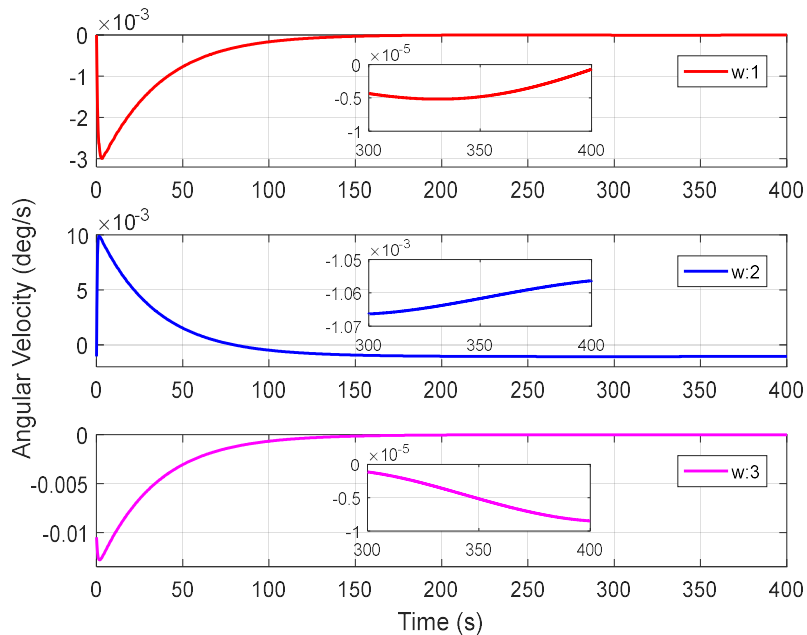


Fig 5.9: Angular velocity using only PD control.

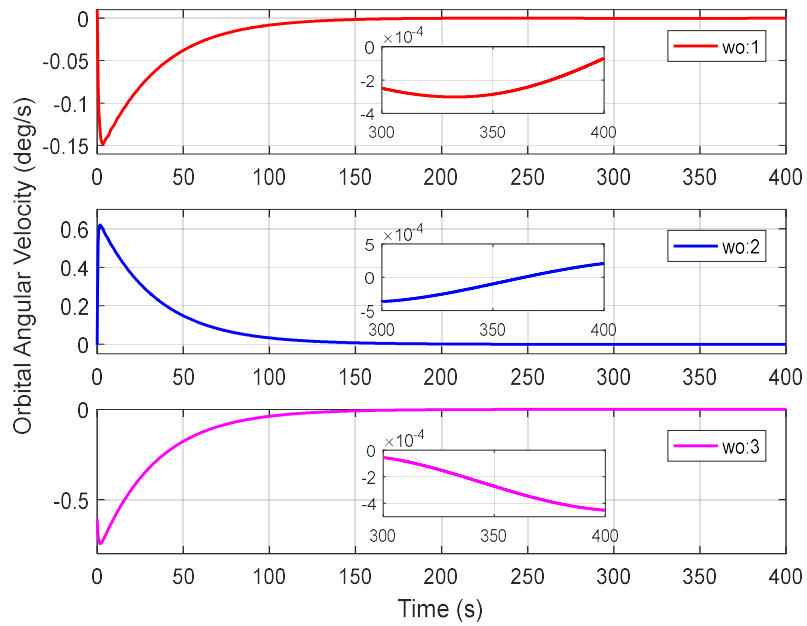


Fig 5.10: Orbital angular velocity using only PD control.

Fig 5.9 and 5.10 show the time responses of the system's angular and orbital angular velocities. These results demonstrate the system's response delay before stabilizing the flexible satellite.

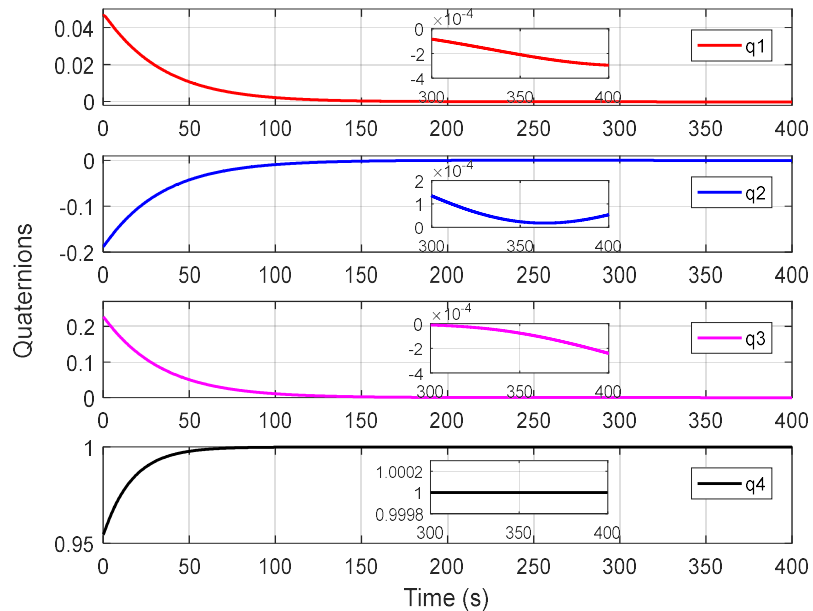


Fig 5.11: Quaternions using only PD control.

Fig 5.11 shows the time response of the attitude angles for a system controlled using only a proportional-derivative (PD) control strategy. The plot depicts the system's response over time in terms of the quaternion components. While the convergence of the quaternion values to steady-state indicates stable behavior, the system can be further improved.

The second simulation includes improvements to the PD controller's gains, achieved by applying the PSO method for optimization.

The system's response to the enhancement control parameters is depicted in the following figures:

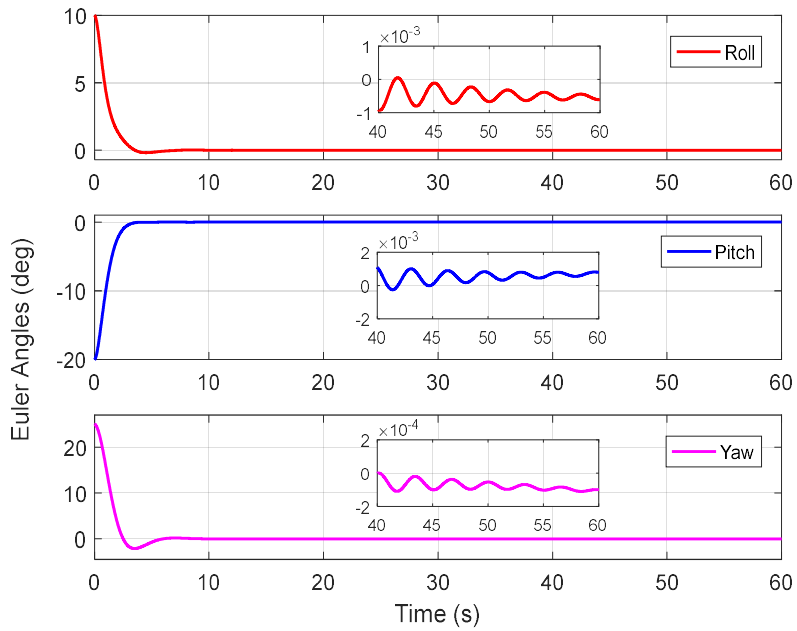


Fig 5.12: Euler angles (IPD).

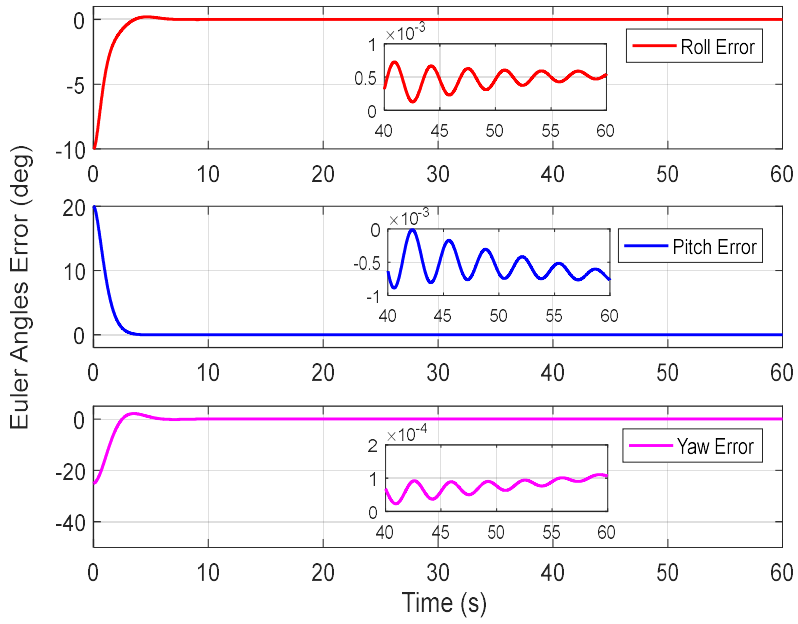


Fig 5.13: Euler angles error (IPD).

Fig 5.12 and 5.13 illustrate the temporal evolution of the spacecraft's orientation, represented by both Euler angles and quaternions, respectively, when employing an improved proportional-derivative control strategy. These plots depict the system's response over time, showcasing how the orientation parameters (Euler angles and quaternion components) converge toward their desired values under the influence of the improved PD controller. It is observed that all three angles accurately follow the reference trajectory, with a settling time of $\langle 3.2139 \quad 3.004 \quad 5.246 \rangle$ s and errors under $4.5 \times 10^{-4}^\circ$ which is seen in Fig 5.13 where the Euler angles error reduce to zero.

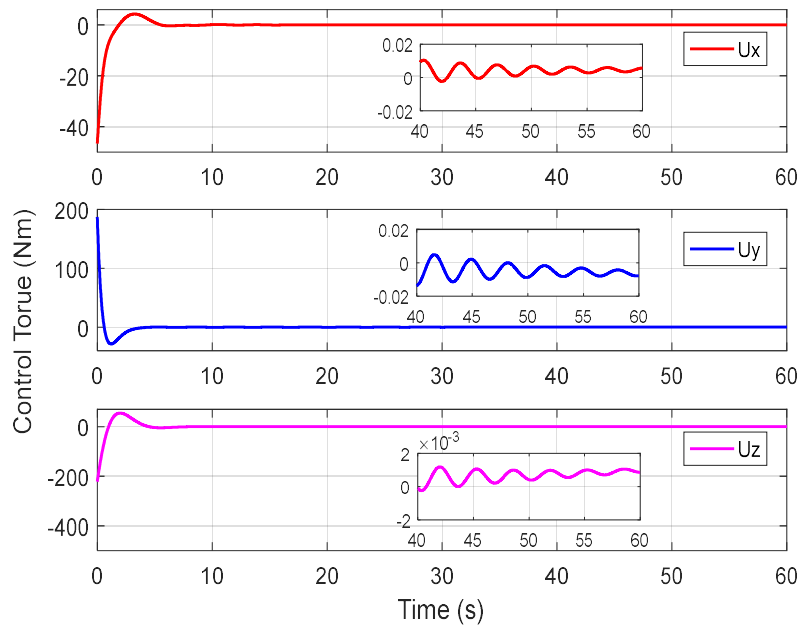


Fig 5.14: Control torque (IPD).

Fig 5.14 represents the control torque acting on the system. The signal initially exhibits an overshoot in amplitude, which then stabilizes at 4.9713 s, 3.0643 s and at 4.1657s for u_x , u_y , u_z respectively with a maximum value of $\{4.648 - 27.9 \text{ } 55.1\}$ Nm.

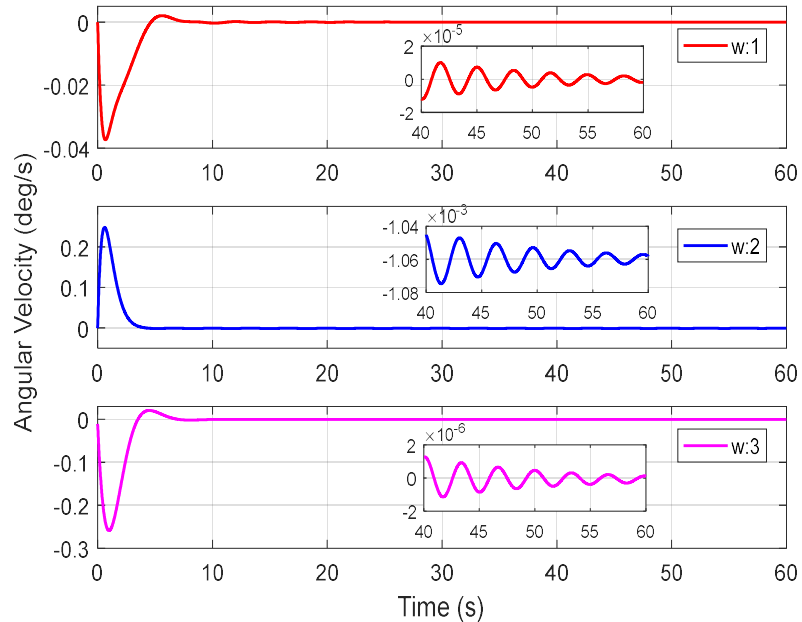


Fig 5.15: Angular velocity (IPD)

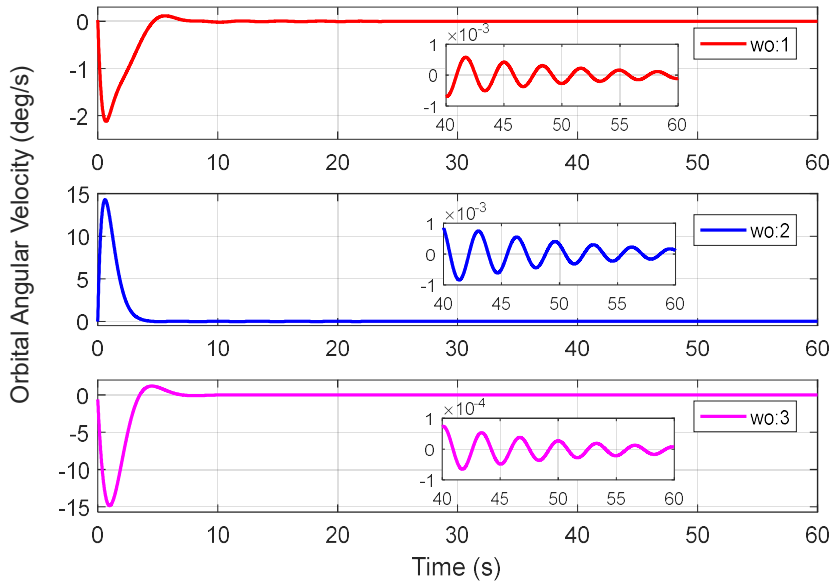


Fig 5.16: Orbital angular velocity (IPD).

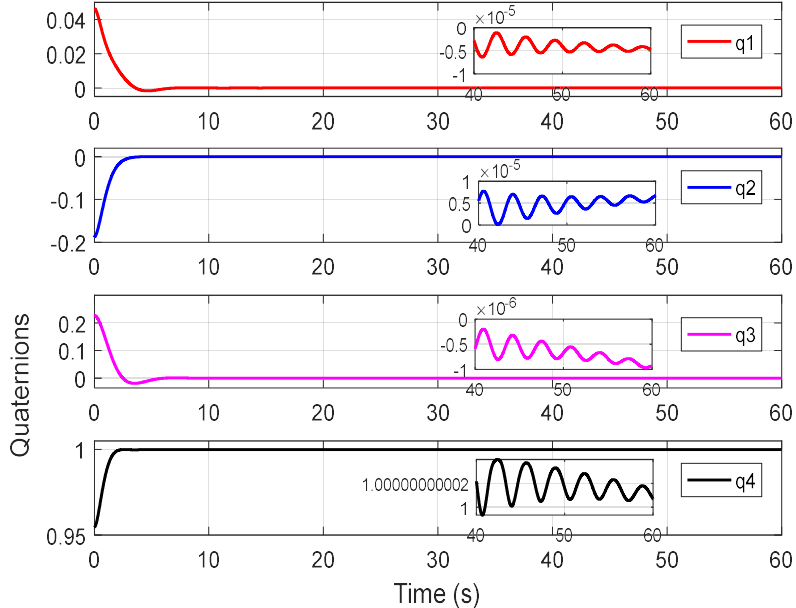


Fig 5.17: Attitude angle using quaternions representation (IPD).

Fig 5.15, Fig 5.16, and Fig 5.17 represent the time responses of the system's angular velocity, orbital angular velocity, and quaternion. Initially, the angular velocity and rotational speed vary, then stabilize around 0 deg/s when the attitude trajectory gets closer to the desired reference.

The most convenient performance metric for evaluating the attitude controller's accuracy is the root mean square (RMSE) of the attitude error. The table shows the RMSE for the roll, pitch, and yaw axes and their rates.

Table 5.3: Root mean square error without DOBC.

	PD	IPD
RMSE ϕ (deg)	0.03383	0.001083
RMSE θ (deg)	0.006226	0.0003859
RMSE ψ (deg)	0.02766	0.001266
RMSE $\dot{\phi}$ (deg/s)	6.982e-05	3.855e-06
RMSE $\dot{\theta}$ (deg/s)	0.0002091	1.024e-05
RMSE $\dot{\psi}$ (deg/s)	0.0004513	1.479e-05

The third part of the simulation demonstrates the performance of the control system when incorporating a Disturbance Observer to estimate the lumped disturbances acting on the system.

5.5.2. Spacecraft model with the Disturbance Observer

Fig 5.18 and Fig 5.19 represent the disturbances estimation and the disturbances errors estimated by Disturbance Observer. It is observed that the disturbances are accurately estimated by the DO, with errors under 4.5×10^{-4} .

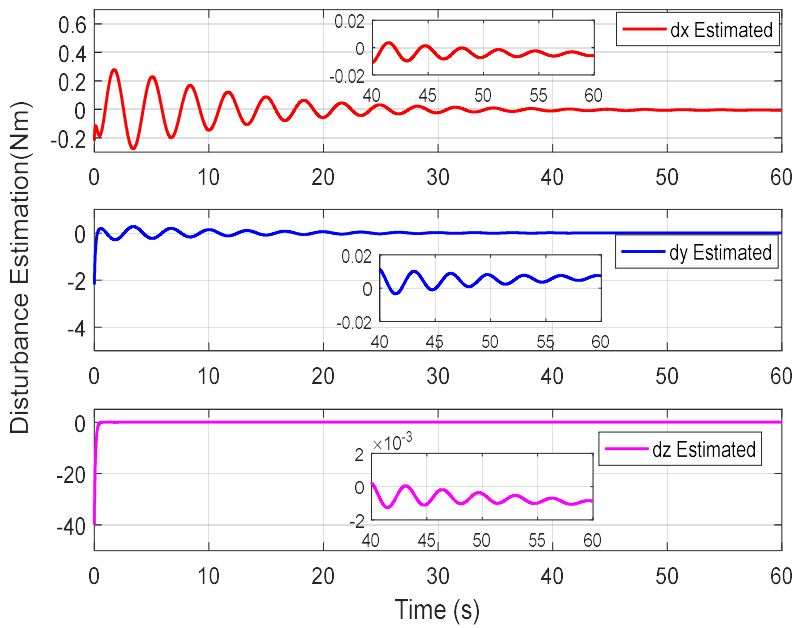


Fig 5.18: Disturbance estimation (IPD-DOBC).

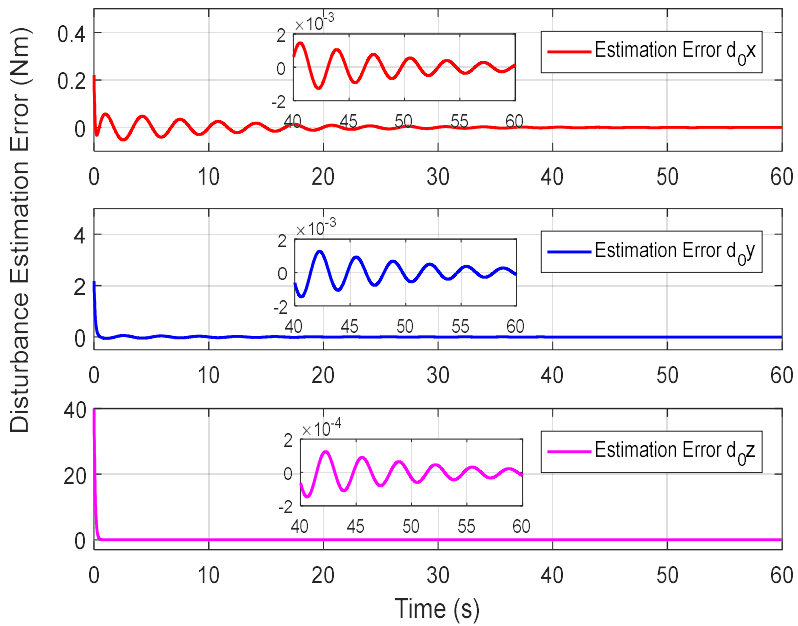


Fig 5.19: Disturbance estimation error (IPD-DOBC).

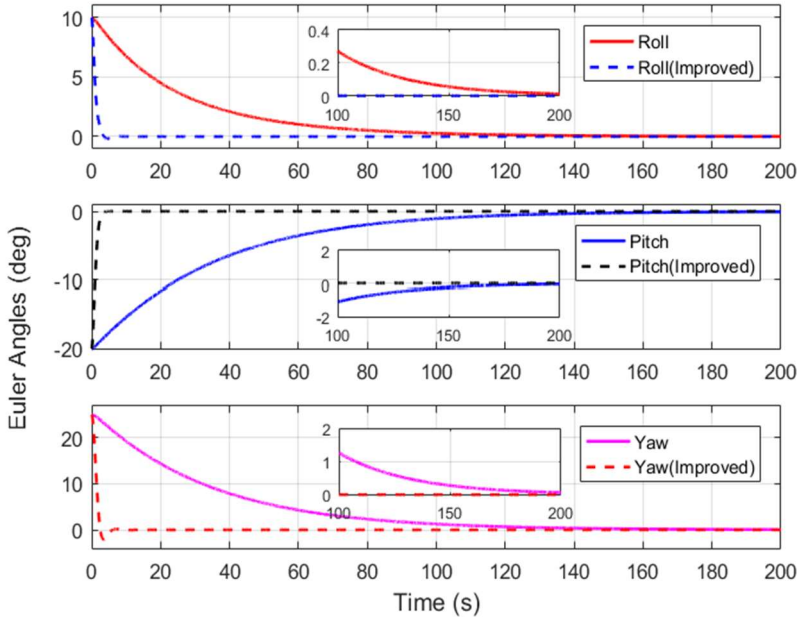


Fig 5.20: Euler angles (IPD-DOBC).

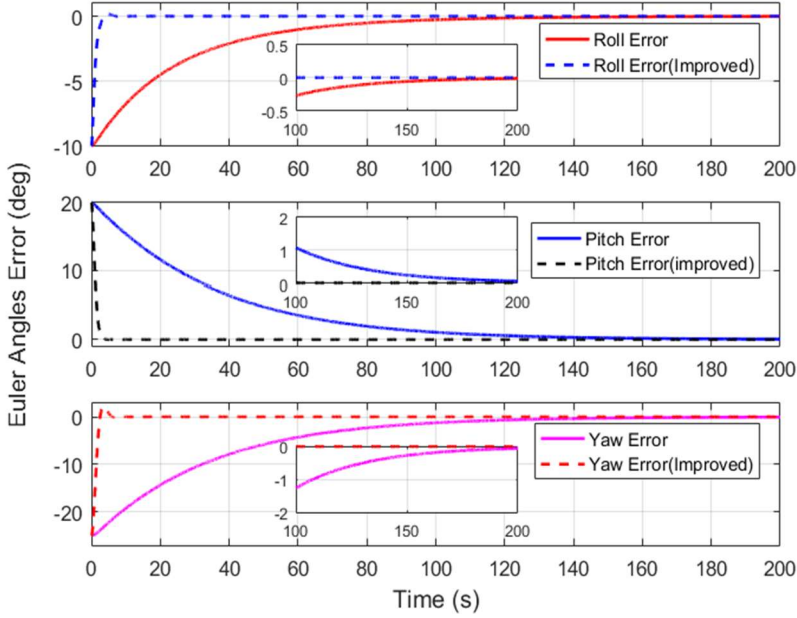


Fig 5.21: Euler angles error (IPD-DOBC).

Fig 5.20 and Fig 5.21 represent the time response of the attitude Euler angles and Euler angles errors. We observe that Euler angles obtained by the improved composite controller follow the reference trajectory and the convergence increased comparing with the PD controller also, the angles errors are reduced to zero. In addition, an improvement in the settling time has been seen where they became: $\langle 3.1913 \ 2.9893 \ 5.2631 \rangle$ s. The performances are clearly presented in the table below containing the RMSE of the Euler angles and their velocities.

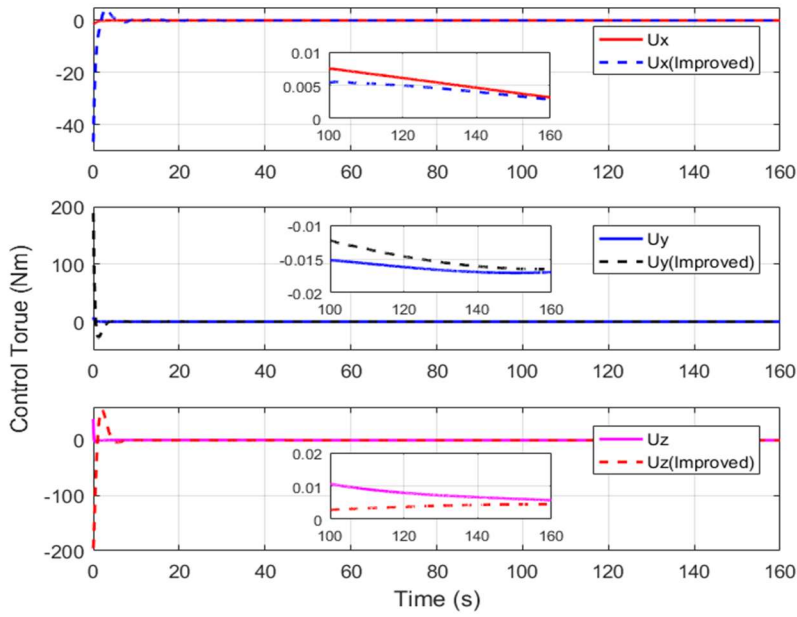


Fig 5.22: Control torque (IPD-DOBC).

The control torque of improved controller has a peak in the response, this is due to the speed of convergence, where the maximum values of control torque for the x, y, and z axes are $\langle 4.638 \quad 188.9 \quad 54.8 \rangle$ Nm respectively as observed in Fig 5.22.

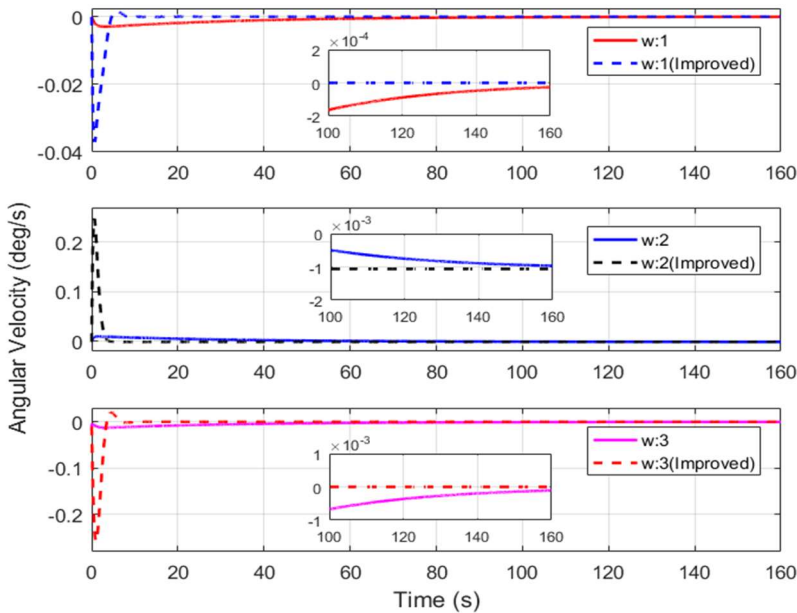


Fig 5.23: Angular velocity (IPD-DOBC).

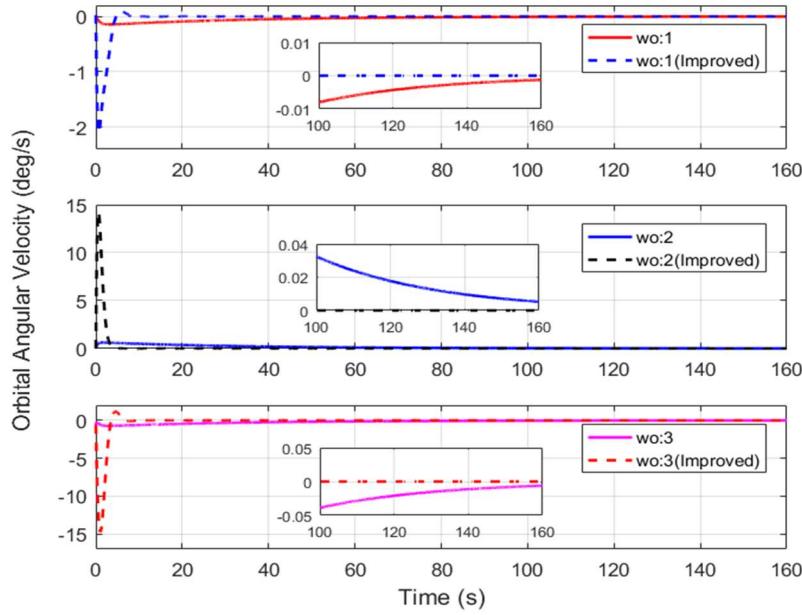


Fig 5.24: Orbital angular velocity (IPD-DOBC).

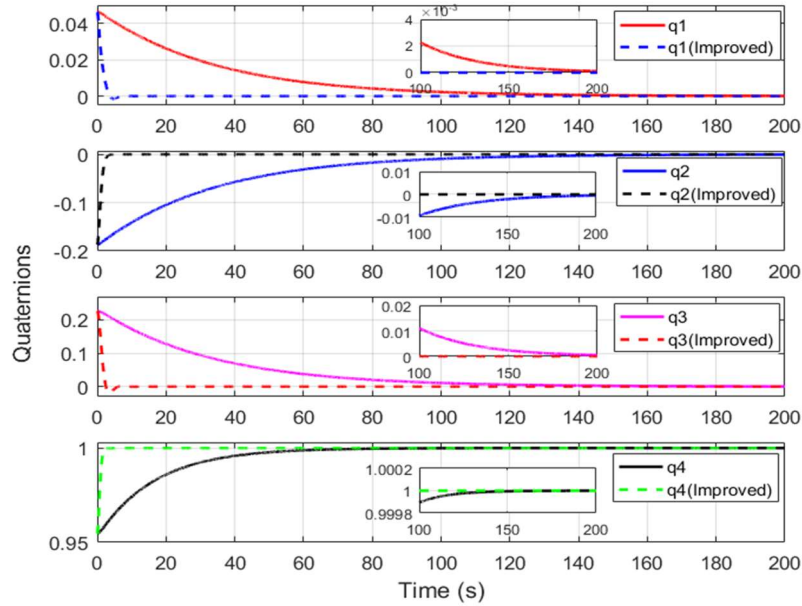


Fig 5.25: Attitude angles using quaternions representation (IPD-DOBC).

Fig 5.23 and Fig 5.24 show the evolution of the angular velocity and the orbital rotation rate, and Fig 5.25 represent the evolution of the Quaternions where an improvement in response is observed.

Table 5.4 shows the RMSE in terms of roll, pitch, and yaw axes and their rates using the composite controller.

Table 5.4: Root mean square error with DOBC.

	Composite controller	Improved composite controller
RMSE ϕ (deg)	0.01181	9.698e-06
RMSE θ (deg)	0.0517	1.119e-05
RMSE ψ (deg)	0.05875	1.617e-06
RMSE $\dot{\phi}$ (deg/s)	0.0003662	5.02e-05
RMSE $\dot{\theta}$ (deg/s)	0.001565	6.725e-05
RMSE $\dot{\psi}$ (deg/s)	0.001802	5.478e-06

The main purpose of the static Monte Carlo simulation is to evaluate and analyze the controller performance. It consists of 9261 iterations with random inputs (Euler angles $\pm 5^\circ$, angular velocities $\pm 10^\circ/\text{sec}$ for roll and the other two $\pm 1^\circ/\text{sec}$). In the light of the results obtained, we note that the convergence of the composite controller is verified for all 9261 iterations. The simulation results, i.e. the error in estimating the Euler angles and their rates of the proposed controller, are presented in the form of a histogram.

The histograms of attitude error standard deviation and attitude velocities for the 9261 Monte-Carlo iterations are shown in the figures below. The figures further confirm that the attitude control system is robust with regard to the variation of the most critical parameters.

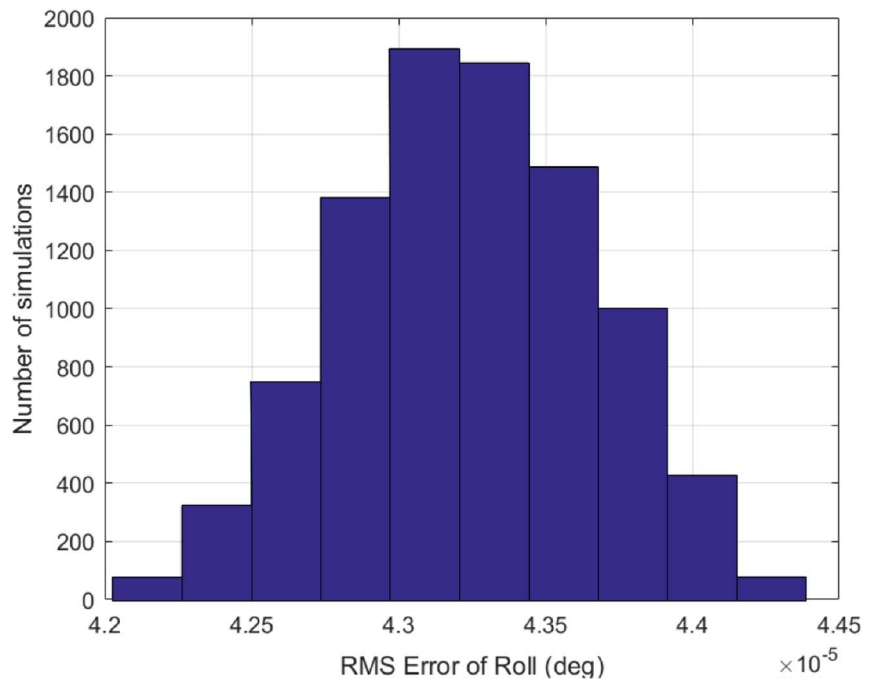


Fig 5.26: Root mean square error of roll.

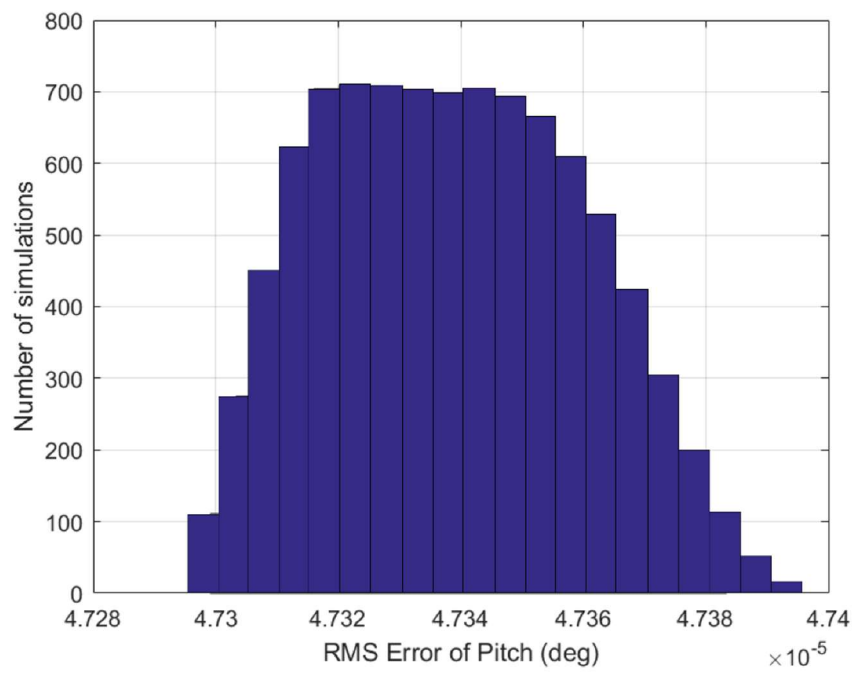


Fig 5.27: Root mean square error of pitch,

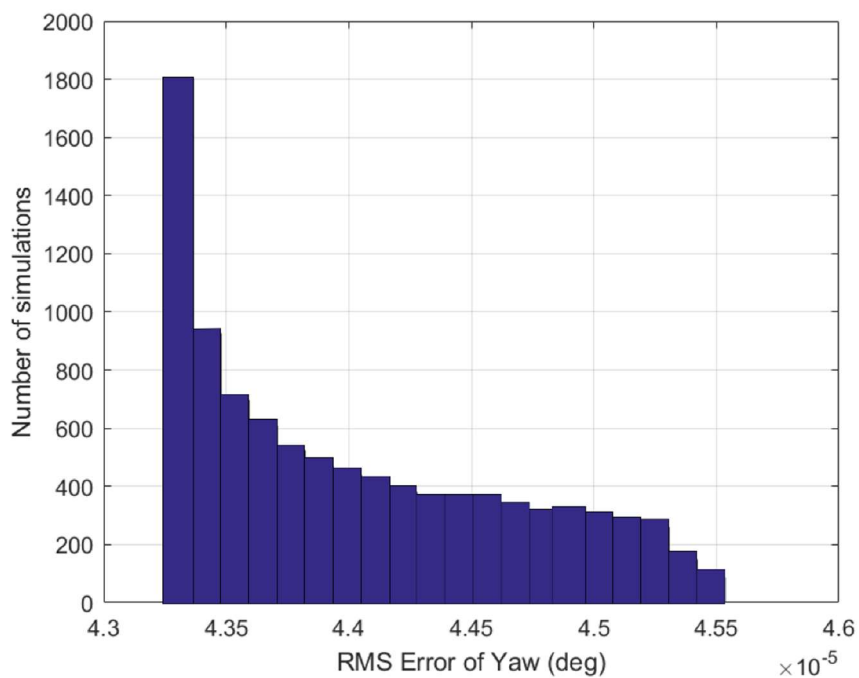


Fig 5.28: Root mean square error of yaw.

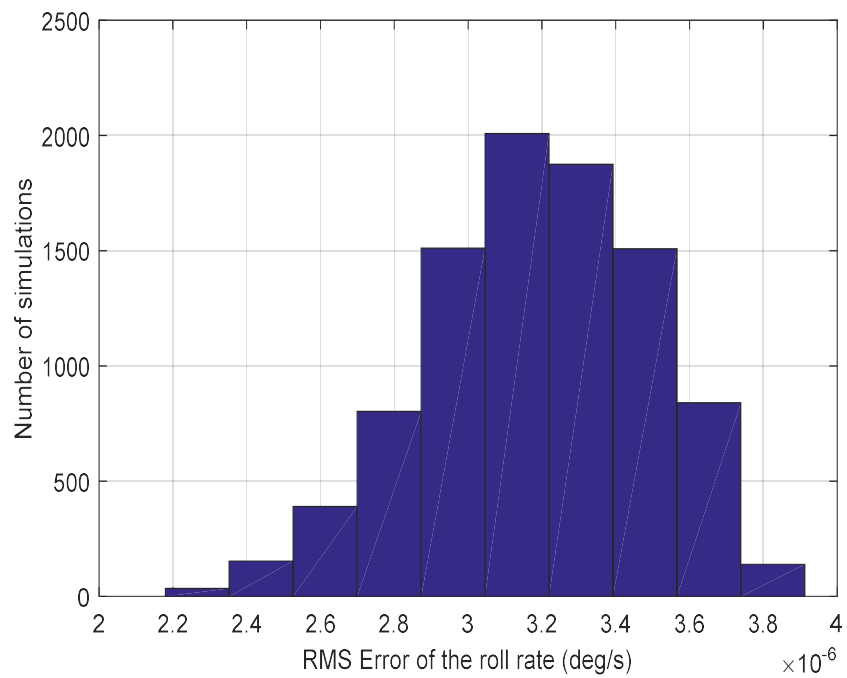


Fig 5.29: Root mean square error of the roll velocity.

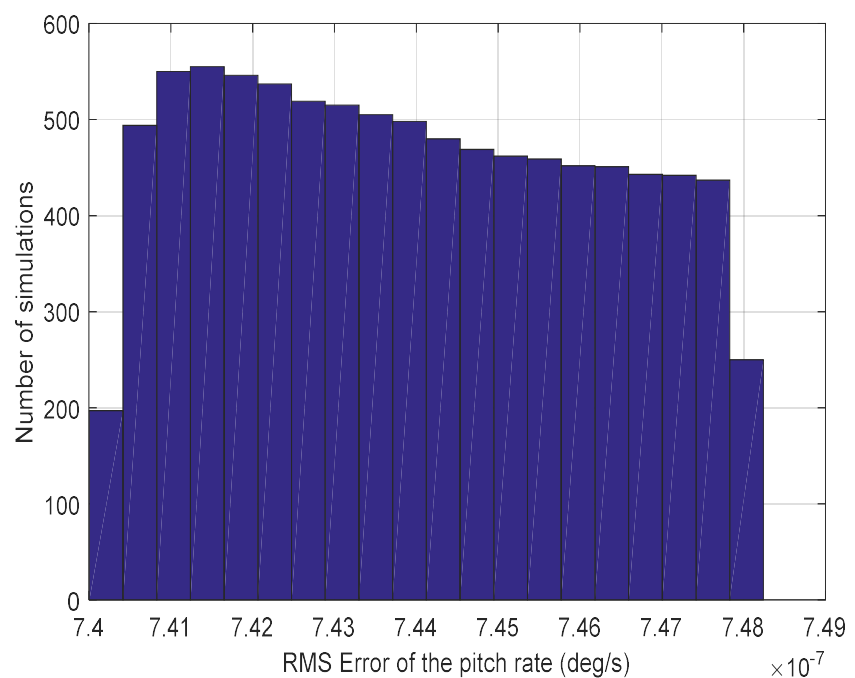


Fig 5.30: Root mean square error of the pitch velocity.

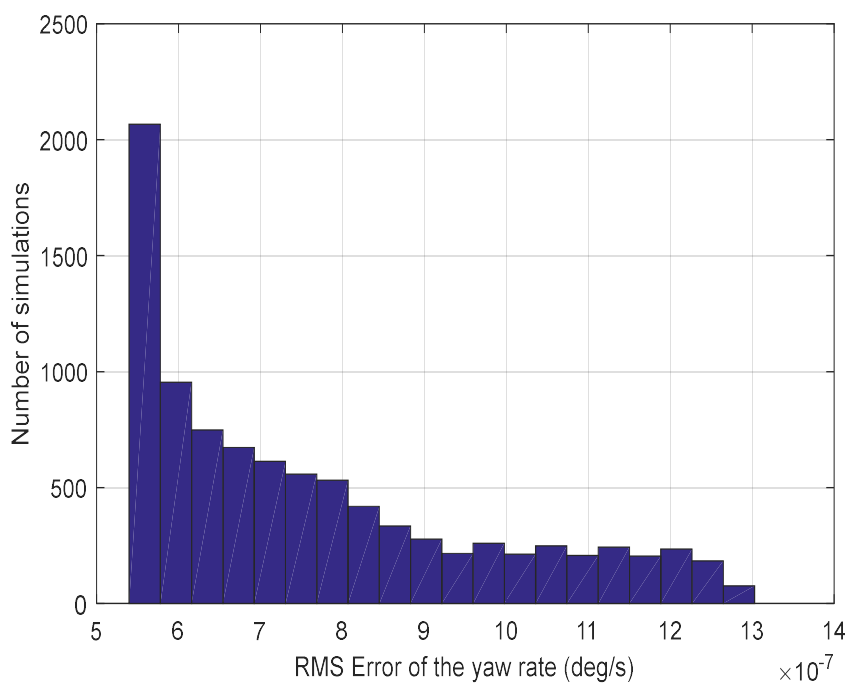


Fig 5.31: Root mean square error of the yaw velocity.

5.6. Conclusion

In this chapter, we analyzed the application of Proportional-Derivative control and Disturbance Observer-Based Control to the attitude stabilization of a flexible spacecraft using quaternion representations. With its simplicity and ease of implementation, PD control provided a baseline for stabilization performance. However, its limitations in handling significant disturbances and model uncertainties were evident. Initially, we attempted to improve the performance of the PD controller by tuning its gains using Particle Swarm Optimization. Simulation results demonstrated the improvements achieved by this method, but it was still limited against the unwanted torques caused by the flexible spacecraft.

To address these limitations, we integrated DOBC under the name composite control, which effectively estimated and compensated for the total disturbances (external and internal), improving the overall robustness and stability of the control system. The fine-tuning of controller parameters using PSO further optimized the performance of both PD and DOBC controllers. PSO proved to be an efficient optimization tool that ensures the best possible control results by systematically identifying optimal parameter sets. In the next chapter, we will investigate an adaptive method to improve the accuracy of the employed method further. The method uses the well-known robust control technique, the sliding mode control approach.

Adaptive Sliding Mode Control with Disturbance Observer for Flexible Spacecraft Attitude Maneuvers under Multiple Disturbances

6. Adaptive Sliding Mode Control with Disturbance Observer for Flexible Spacecraft Attitude Maneuvers under Multiple Disturbances

6.1 Introduction:

This chapter investigates advanced control techniques for spacecraft attitude stabilization under multiple disturbances, both internal (vibration disturbance torques caused by solar panels) and external (caused by solar radiation), building upon the principles established by PD and DOBC methods. The focus is on sliding mode control (SMC), a robust control strategy for effectively attenuating system uncertainties and external disturbances. SMC offers superior tracking precision and enhanced stability compared to traditional methods. However, the chattering phenomenon often accompanies it, causing unwanted high-frequency oscillations in the control inputs. Consequently, addressing the chattering issue is crucial to realizing the full potential of SMC in spacecraft attitude control applications.

To further enhance robustness and address the limitations of conventional Sliding Mode Control, this chapter introduces Adaptive Sliding Mode Control (ASMC), an advanced variant of SMC. This adaptive approach employs dynamic real-time adjustment of control parameters, enabling improved performance and robustness across varying operating conditions. By incorporating adaptive mechanisms, ASMC aims to refine the control response, mitigate the detrimental effects of chattering, and achieve superior overall system stability.

To further enhance the control system's performance, we employ Particle Swarm Optimization to tune the control parameters, ensuring the system achieves the highest possible accuracy and robustness against multiple disturbances.

6.2. Sliding mode controller design

Sliding mode is a nonlinear control technique for variable-structure systems. Its properties include precision, robustness, ease of adjustment, and simplicity of implementation.

The main idea of sliding mode control is to drive the system states to a suitably selected region, find a convergence condition allowing the system to converge on the sliding surface, and then design a control law that will always keep the system in this region. In other words, a sliding mode control is designed in three stages:

- Choice of sliding surface.
- Formulation of convergence existence conditions.
- Establishing the control law.

6.2.1. Choice of sliding surface

The choice of sliding surface depends on the application, the desired performance, and the objective. The aim is to keep surface S equal to zero and ensure that the system's trajectory remains on the surface at all times.

6.2.2. Formulation of convergence existence conditions

The conditions of existence and convergence are the factors that allow the various dynamics of the system to converge towards the sliding surface. There are two considerations to ensure the convergence mode.

a. The attractiveness (Reaching condition)

For the trajectories to converge on the sliding surface, the vectors S and \dot{S} must have opposite signs, which means that:

$$S\dot{S} < 0 \quad (6.1)$$

Or

$$\begin{cases} \dot{S} > 0 & \text{when } S < 0 \\ \dot{S} < 0 & \text{when } S > 0 \end{cases} \quad (6.2)$$

b. Lyapunov function

This involves choosing a candidate Lyapunov function $V > 0$ (positive scalar function), and choose a control law that will decrease this function $\dot{V} < 0$.

By establishing, for example, a Lyapunov candidate function as follows

$$V = \frac{1}{2}S^2 \quad (6.3)$$

By deriving Eq (6.3), we obtain:

$$\dot{V} = S\dot{S} \quad (6.4)$$

For the Lyapunov candidate function to decrease, it is sufficient to ensure that:

$$\dot{V} < 0 \quad (6.5)$$

6.2.3. Establishing the control law

The sliding mode control is composed of two terms. A continuous term, called equivalent control, and a discontinuous term, called switching control.

$$u = u_{eq} + u_{sw} - \hat{d} \quad (6.6)$$

The equivalent control u_{eq} is determined by assuming that the derivative of the sliding surface is zero $\dot{S} = 0$.

The switch control u_{sw} force the system condition won't come out of the sliding surface. The easiest form this command can take is :

$$u_{sw} = -K_1 \text{sign}(S) - K_2 S \quad (6.7)$$

where

K_1, K_2 are positive gains

$$\text{sign}(S) = \begin{cases} 1 & S > 0 \\ -1 & S < 0 \end{cases} \quad (6.8)$$

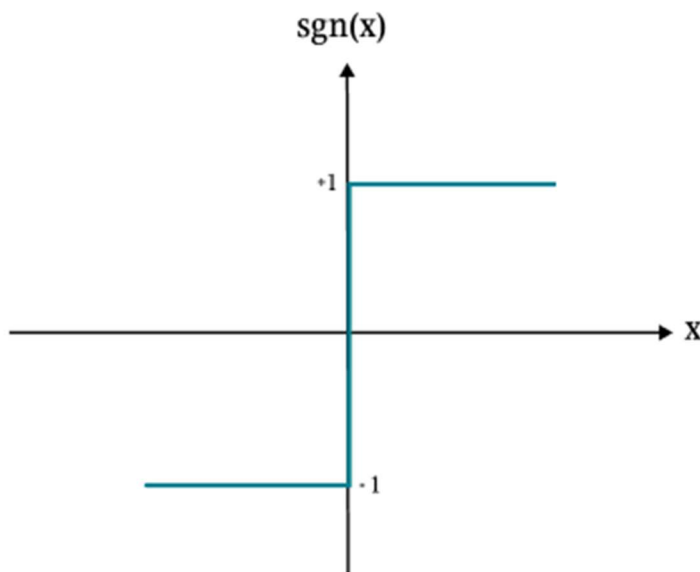


Fig 6.1: Sign function.

Using the *sign* function means the u_{sw} command switches between two values $\pm K_1$. The discontinuity applied to this control can lead to high-frequency oscillations of the system

trajectory around the sliding surface during the sliding regime, which causes the phenomenon of chattering.

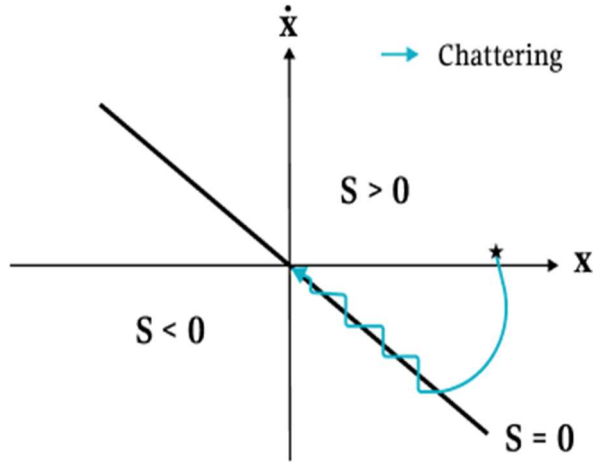


Fig 6.2: Chattering phenomenon.

Chattering must be minimized or removed for the controller to function properly because this phenomenon can damage actuator components significantly. This can be done by smoothing the control discontinuity in a thin boundary layer next to the switching surface. To achieve it, various techniques have been suggested, such as:

Saturation function

It consists in approximating the discontinuous command by a continuous law in the proximity of the surface ; this function is called "sat".

$$sat(S) = \begin{cases} -1 & \text{for } S < -\varepsilon \\ \frac{S}{\varepsilon} & \text{for } |S| \leq \varepsilon \quad \text{where } \varepsilon > 0 \\ 1 & \text{for } S > \varepsilon \end{cases} \quad (6.9)$$

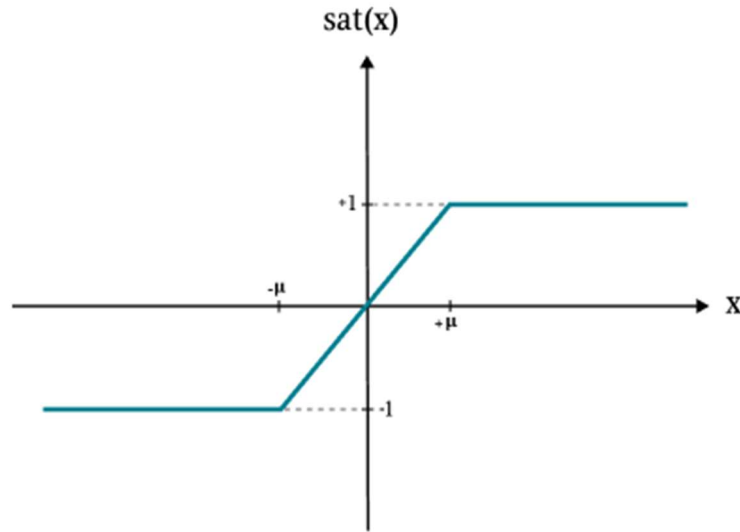


Fig 6.3: Sat function.

The Hyperbolic tangent function

A trigonometric function that helps to smooth the response of the control law.

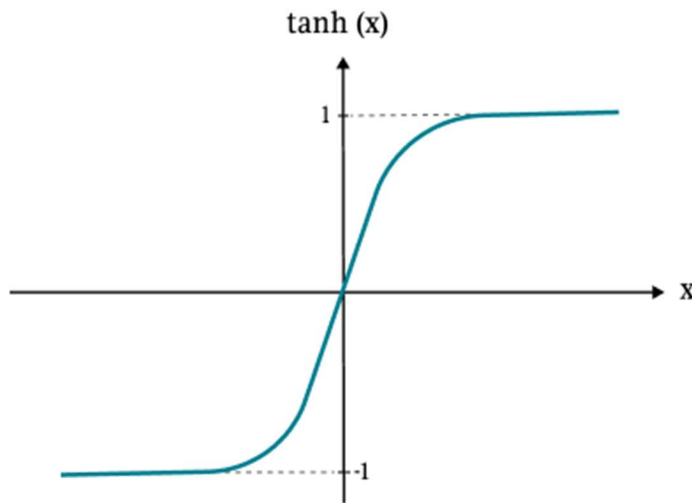


Fig 6.4: Tanh function.

6.3. Application of sliding mode attitude control of flexible spacecraft under multiple disturbances

This part focuses on designing a sliding mode control law to guarantee the system's stability, as Chapter 5, Eq (5.2) describes. The design strategy concerns two main steps. First, a disturbance observer is constructed to estimate the combined effects of all disturbances, including internal disturbances acting on the system. Second, a disturbance observer-based sliding mode control approach is developed. In this approach, a suitable control effort is derived to drive the system states towards the sliding mode surface, ensuring stability is achieved.

First, define the switch surface that the sliding various structures control requires. The switch surface function can be written as follows based on the spacecraft's attitude mathematical model:

$$S = \omega_e + k q_{ve} \quad (6.10)$$

where k is a 3×3 symmetric positive-definite constant matrix, $q_v = [q_{e1} \quad q_{e2} \quad q_{e3}]^T$ and ω_e is the angular velocity error.

Assuming the desired attitude angular velocity is ω_d , then the error of attitude angular velocity can be defined as:

$$\omega_e = \omega - \omega_r \quad (6.11)$$

where $\omega_r = R(q_e) \omega_d$, $R(q_e)$ denotes the transition matrix from orbit coordinate system to body coordinate system which based on the description of error quaternion. The expression is as follow:

$$R(q_e) = (q_{e4}^2 - q_{ve}^T q_{ve}) I_3 - 2(q_{e4} q_{ve}^\times - q_{ve} q_{ve}^T) \quad (6.12)$$

Besides:

$$\dot{\omega}_r = R(q_e) \dot{\omega}_d - \omega_e^\times R(q_e) \omega_d \quad (6.13)$$

Deriving Eq (6.11) we get:

$$\dot{S} = \dot{\omega}_e + k \dot{q}_{ve} \quad (6.14)$$

Recall that the control law is divided into two parts:

$$u = u_{eq} + u_{sw} - \hat{d} \quad (6.15)$$

The control u_{eq} is determined when the sliding regime is reached, where the surface S and its derivative are null.

By substituting Eq (2.8) and Eq (6.14) into Eq (6.15) we can get the following result:

$$u_{eq} = J\dot{\omega}_d + \omega^\times J\omega - Jk\dot{q}_{ve} \quad (6.16)$$

The final control law is:

$$u = J\dot{\omega}_d + \omega^\times J\omega - Jk\dot{q}_{ve} - K_1 sign(S) - K_2 S - \hat{d} \quad (6.17)$$

In order to prove the stability of the system, a Lyapunov candidate function can be considered as

$$V = \frac{1}{2} S^T J S \quad (6.18)$$

Derivate Eq (6.16), can get the following result:

$$\dot{V} = S^T J \dot{S} = S^T J (\dot{\omega}_e + k \dot{q}_{ve}) = S^T (-J \dot{\omega}_d - \omega^\times J \omega + u + Jk \dot{q}_{ve}) \quad (6.19)$$

By substituting Eq (6.15) in Eq (6.17) we get:

$$\dot{V} = S^T J \dot{S} = S^T (-\hat{d} - K_1 \text{sign}(S) - K_2 S) < 0 \quad (6.20)$$

Since \dot{V} is negative definite then the asymptotic stability has been proved.

The next section will present the proposed adaptive sliding mode controller and provide a stability analysis to demonstrate the robustness of the resulting closed-loop system. However, it is important to note that while this controller offers advantages, it is unable to effectively suppress vibration disturbance torques.

6.4. Adaptive sliding mode attitude control design

As mentioned before, the main purpose of this chapter is to propose a control design for the attitude control of flexible spacecraft. It is well known that an adaptive sliding mode control (ASMC) method is presented based on an observer, in which two adaptive laws are proposed and designed to adjust the parameter gains and to guarantee the response of the spacecraft attitude control system. As we know, SMC is a robust method for controlling nonlinear and uncertain systems, which has attractive features to make the systems insensitive to uncertainties on the sliding surface.

To solve the attitude tracking problem with disturbances existing in the spacecraft system, the adaptive method is a suitable choice and has been widely applied. Therefore, in order to reduce the effect of disturbances, the SMC scheme can be considered to reach the goal with the combination of the adaptive approach. Various methods for adaptive sliding mode control aim to enhance system robustness and performance by dynamically adjusting control parameters to respond to system uncertainties, internal and external disturbances.

6.4.1. Method 1

The first control laws are designed and formulated as follows:

$$u_i = -\frac{u_m S_i}{|S_i| + \rho^2 \sigma} \quad i = 1, 2, 3 \quad (6.21)$$

$$S = \omega_e + \rho^2(t) q_{ve} \quad (6.21)$$

where S_i is the i th element of S defined in Eq (6.21), $\rho(t)$ is a time-varying function that will be defined later and σ is a positive control constant.

The following candidate Lyapunov function is given by

$$V = \frac{1}{2}[\omega_e^T J \omega_e + 2\rho^2(q_{ve}^T q_{ve} + (q_{e4} - 1)^2) + \rho^2/\gamma] \quad (6.22)$$

Its derivative along the motions of the system yields

$$\dot{V} = -\omega_e^T H \omega - \omega^T g + \omega^T u + \omega^T v + \rho \dot{\rho} \left[\frac{1}{\gamma} + 4(1 - q_{e4}) \right] + \rho^2 q_{ve}^T \omega \quad (6.23)$$

$$\begin{aligned} \dot{V} = & -u_m \sum_{i=1}^3 \frac{\omega_{ie}^2 + \rho^2 \omega_{ie} q_{vei}}{|S_i| + \rho^2 \sigma} + \omega_e^T (-g + v) + \rho \dot{\rho} \left[\frac{1}{\gamma} + 4(1 - q_{e4}) \right] + \rho^2 q_{ve}^T S \\ & - \rho^4 q_{ve}^T q_{ve} \end{aligned} \quad (6.24)$$

where $H = (R(q_e)\omega_d)^\times J + J(R(q_e)\omega_d)^\times$ and $g = (R(q_e)\omega_d)^\times JR(q_e)\omega_d + JR(q_e)\dot{\omega}_d$ and v an auxiliary variable and it is assumed that $v(t) = \{v : |v| = |v_1| + |v_2| + |v_3| \leq \bar{v}\}$.

It is noted that the following holds:

$$\begin{aligned} \frac{\omega_{ie}^2}{|S_i| + \rho^2 \sigma} &= \frac{\omega_{ie}^2}{|\omega_{ie} + \rho^2(t)q_{vei}| + \rho^2 \sigma} \geq \frac{\omega_{ie}^2}{|\omega_{ie}| + \rho^2(1 + \sigma)} \\ &= |\omega_{ie}| \left(1 - \frac{\rho^2(1 + \sigma)}{|\omega_{ie}| + \rho^2(1 + \sigma)} \right) \end{aligned} \quad (6.25)$$

Hence,

$$\begin{aligned} \dot{V} &\leq -|\omega_e|(u_m - |g| - \bar{v}) \\ &+ u_m \sum_{i=1}^3 \left[\frac{|\omega_{ie}| \rho^2(1 + \sigma)}{|\omega_{ie}| + \rho^2(1 + \sigma)} - \frac{\rho^2 \omega_{ie} q_{vei}}{|S_i| + \rho^2 \sigma} \right] + \rho \dot{\rho} \left[\frac{1}{\gamma} + 4(1 - q_{e4}) \right] \\ &+ \rho^2 q_{ve}^T S - \rho^4 q_{ve}^T q_{ve} \end{aligned} \quad (6.26)$$

The adapting law for $\rho(t)$ is chosen as

$$\dot{\rho} = \frac{\gamma \rho}{1 + 4\gamma(1 - q_{e4})} \left\{ u_m \sum_{i=1}^3 \left[\frac{\omega_{ie} q_{vei}}{|S_i| + \rho^2 \sigma} - \frac{|\omega_{ie}|(1 + \sigma)}{|\omega_{ie}| + \rho^2(1 + \sigma)} \right] - q_{ve}^T S \right\} \quad (6.27)$$

which results in

$$\dot{V} \leq -|\omega_e|(u_m - |g| - \bar{v}) - \rho^4 q_{ve}^T q_{ve} \quad (6.28)$$

Since the available control is sufficient to reject disturbances and simultaneously track the desired trajectory, this implies that $\dot{V} \leq 0$ and ω_e , ρ are bounded. and q_{ve} and q_{e4} are bounded. Also ω_e is bounded, so V is bounded. [55, 56]

6.4.2. Method 2

As the second part of this section, the composite control law design for flexible spacecraft attitude control with multiple disturbances is presented as follows:

Assumption 1: the lumped disturbances d is assumed to be bounded and satisfy the following condition:

$$\|d\| \leq c_{01} + k_1 \|q_{ve}\| + k_{02} \|\omega_e\| \quad (6.29)$$

where c_{01} , k_1 , and k_{02} are unknown bounds, which are not easily obtained due to the complicated structure of uncertainties in practical systems. [57, 58]

Assumption 2: there exist positive scalar c and k_2 such that the following condition is satisfied:

$$\begin{aligned} & \left[\left\| (\bar{k}q_{ve} - R(q_e)\omega_d)^\times \right\| + \frac{1}{2} \bar{k} \|q_{e4}I_3 + q_{ve}^\times\| + \|R(q_e)\omega_d\| \right] \|J\| \|\omega_e\| \\ & + \left\| (\bar{k}q_{ve} - R(q_e)\omega_d)^\times J R(q_e)\omega_d - J R(q_e)\dot{\omega}_d \right\| \\ & \leq (k_2 - k_{02}) \|\omega_e\| + (c - c_{01}) \end{aligned} \quad (6.30)$$

The control law is modified as

$$u = -\tau S - \bar{\sigma} sign(S) - u_p - \hat{d} \quad (6.31)$$

And

$$u_p = \begin{cases} \frac{S}{\|S\|} \hat{\rho}, & \text{if } \hat{\rho} \|S\| > \epsilon \\ \frac{S}{\epsilon} \hat{\rho}^2, & \text{if } \hat{\rho} \|S\| \leq \epsilon \end{cases} \quad (6.32)$$

And the adaptation updates laws are

$$\hat{\rho} = \hat{c}(t) + \hat{k}_1(t) \|q_{ve}\| + \hat{k}_2(t) \|\omega_e\| \quad (6.33)$$

$$\dot{\hat{c}}(t) = p_0(-\epsilon_0 \hat{c}(t) + \|S\|) \quad (6.34)$$

$$\dot{\hat{k}}_1 = p_1(-\epsilon_1 \hat{k}_1(t) + \|S\| \|q_{ve}\|) \quad (6.35)$$

$$\dot{\hat{k}}_2 = p_2(-\epsilon_2 \hat{k}_2(t) + \|S\| \|\omega_e\|) \quad (6.36)$$

where $p_0, p_1, p_2, \epsilon, \epsilon_0, \epsilon_1$ and ϵ_2 are the design parameters and $\hat{c}, \hat{k}_1, \hat{k}_2$ and $\hat{\rho}$ are used to estimate the bounds.

The following candidate Lyapunov function is given by

$$V = \frac{1}{2} \left[S^T JS + \frac{1}{p_0} \tilde{c}^2 + \frac{1}{p_1} \tilde{k}_1^2 + \frac{1}{p_2} \tilde{k}_2^2 \right] \quad (6.37)$$

where $\tilde{c} = c - \hat{c}(t)$ and $\tilde{k} = k - \hat{k}(t)$. Its time derivation is

$$\dot{V} = S^T J \dot{S} - \frac{1}{p_0} \tilde{c} \dot{\tilde{c}} - \frac{1}{p_1} \tilde{k}_1 \dot{\tilde{k}}_1 - \frac{1}{p_2} \tilde{k}_2 \dot{\tilde{k}}_2 \quad (6.38)$$

Noting the property of operator \cdot^\times that implied that $S^T S^\times = [0 \ 0 \ 0]$, we have

$$\begin{aligned} \dot{V} &= S^T \left[(\bar{k} q_{ve} - R(q_e) \omega_d)^\times J \omega_e + \frac{1}{2} J \bar{k} (q_{e4} I_3 + q_{ve}^\times) \right] \omega_e + S^T J \omega_e^\times R(q_e) \omega_d + \\ &\quad S^T \left[(\bar{k} q_{ve} - R(q_e) \omega_d)^\times J R(q_e) \omega_d - J R(q_e) \dot{\omega}_d \right] + S^T u_{ada} + S^T d - \frac{1}{p_0} \tilde{c} \dot{\tilde{c}} - \\ &\quad \frac{1}{p_1} \tilde{k}_1 \dot{\tilde{k}}_1 - \frac{1}{p_2} \tilde{k}_2 \dot{\tilde{k}}_2 \end{aligned} \quad (6.39)$$

$$\begin{aligned} \dot{V} &\leq \left[\left\| (\bar{k} q_{ve} - R(q_e) \omega_d)^\times \right\| + \frac{1}{2} \bar{k} \|q_{e4} I_3 + q_{ve}^\times\| \right. \\ &\quad \left. + \|R(q_e) \omega_d\| \right] \|J\| \|S\| \|\omega_e\| \\ &\quad + \left\| (\bar{k} q_{ve} - R(q_e) \omega_d)^\times J R(q_e) \omega_d - J R(q_e) \dot{\omega}_d \right\| \|S\| + \|S\| \|d\| \end{aligned} \quad (6.40)$$

$$+ S^T u_{ada} - \frac{1}{p_0} \tilde{c} \dot{\tilde{c}} - \frac{1}{p_1} \tilde{k}_1 \dot{\tilde{k}}_1 - \frac{1}{p_2} \tilde{k}_2 \dot{\tilde{k}}_2$$

where $u_{ada} = -\tau S - \bar{\sigma} sign(S) - u_p$, and noting the Assumption 1 and 2, we obtain

$$\dot{V} \leq \|S\|(c + k_1\|q_{ve}\| + k_2\|\omega_e\|) + S^T u_{ada} - \frac{1}{p_0} \tilde{c} \dot{\tilde{c}} - \frac{1}{p_1} \tilde{k}_1 \dot{\tilde{k}}_1 - \frac{1}{p_2} \tilde{k}_2 \dot{\tilde{k}}_2 \quad (6.41)$$

If $\hat{\rho}\|S\| > \epsilon$, with the control law defined in Eq (3.32) and adaptation laws Eq (3.33), Eq (3.36), we have

$$\begin{aligned} \dot{V} \leq & S^T [-\tau S - \bar{\sigma} sign(S)] - \|S\| (\hat{c}(t) + \hat{k}_1(t)\|q_{ve}\| + \hat{k}_2(t)\|\omega_e\|) \\ & + \|S\| (c + k_1\|q_{ve}\| + k_2\|\omega_e\|) \end{aligned} \quad (6.42)$$

$$\dot{V} \leq -\sum_{i=1}^3 (\tau_i S_i^2 + \bar{\sigma}_i |S_i|) + \frac{1}{4} (\epsilon_0 c^2 + \epsilon_1 k_1^2 + \epsilon_2 k_2^2) \quad (6.43)$$

Clearly $\dot{V} < 0$, and the system is stable.

If $\hat{\rho}\|S\| > \epsilon$, with the control law defined in Eq (3.32) and adaptation laws Eq (3.33), Eq (3.36), we have

$$\begin{aligned} \dot{V} \leq & S^T [-\tau S - \bar{\sigma} sign(S)] - \frac{\|S\|^2}{\epsilon} \hat{\rho}^2 + \|S\| (c + k_1\|q_{ve}\| + k_2\|\omega_e\|) - \\ & \tilde{c}(-\epsilon_0 \hat{c}(t) + \|S\|) - \tilde{k}_1(-\epsilon_1 \hat{k}_1(t) + \|S\| \|q_{ve}\|) - \tilde{k}_2(-\epsilon_2 \hat{k}_2(t) + \|S\| \|\omega_e\|) \end{aligned} \quad (6.44)$$

$$\dot{V} \leq -\sum_{i=1}^3 (\tau_i S_i^2 + \bar{\sigma}_i |S_i|) + \frac{\epsilon}{4} + \frac{1}{4} (\epsilon_0 c^2 + \epsilon_1 k_1^2 + \epsilon_2 k_2^2) \quad (6.45)$$

Through a similar analysis, it can be shown that the system is stable.

Remark: The design parameters ϵ_0 , ϵ_1 and ϵ_2 determine the band of the bounded region, and we can choose them to be small enough to almost guarantee the motion along the sliding surface. However, a trade-off is made between the band of the bounded region and the convergence speed of the estimated bounds \hat{c} , \hat{k}_1 and \hat{k}_2 , which also depend on the parameters ϵ_0 , ϵ_1 and ϵ_2 . Too small ϵ_0 , ϵ_1 and ϵ_2 will lead to a very low convergence rate of the estimated bounds \hat{c} , \hat{k}_1 and \hat{k}_2 . Therefore, the parameters ϵ_0 , ϵ_1 and ϵ_2 cannot be chosen too small. In addition, the chattering can be reduced by a proper tuning of the parameters τ and $\bar{\sigma}$.

6.5. Simulation and result analysis

To validate the effectiveness of the proposed approach, numerical simulations are conducted on a flexible spacecraft model, and the results are presented in this section.

6.5.1 Sliding Mode Control results

- **Using sign function**

To enhance the tuning accuracy of the control parameters, a PSO method is employed for optimizing the controller parameters. In the PSO algorithm implementation, the particle population size is set to 50, the maximum number of iterations is set to 200, and the cognitive and social learning factors are both set to 2.

Table 6.1: Control parameters of the sign function.

Controller part	Control gain	Value
SMC	k	3.45
	K_1	20
	K_2	2.6055

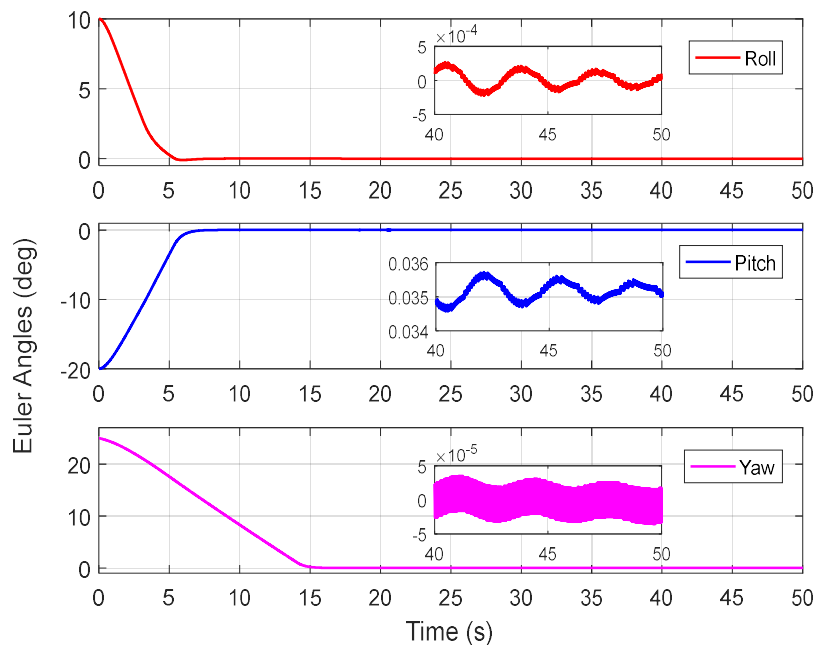


Fig 6.5: Euler angles. (Sign)

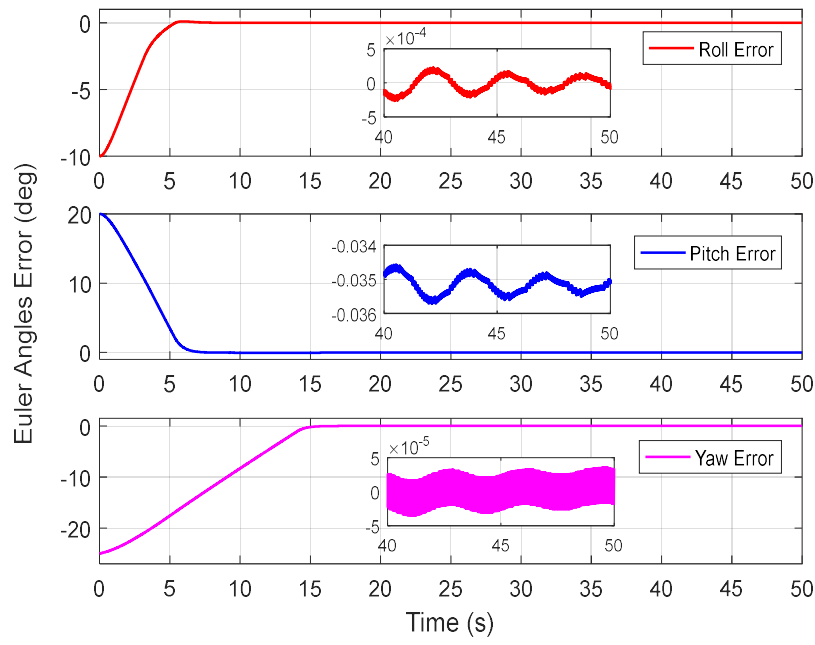


Fig 6.6: Euler angles error. (Sign)

Fig 6.5 demonstrates that the angle errors converge to nearly zero, indicating that the desired angles are achieved. The settling times for the roll, pitch, and yaw angles are 5.0869 seconds, 6.3189 seconds, and 14.5067 seconds, respectively.

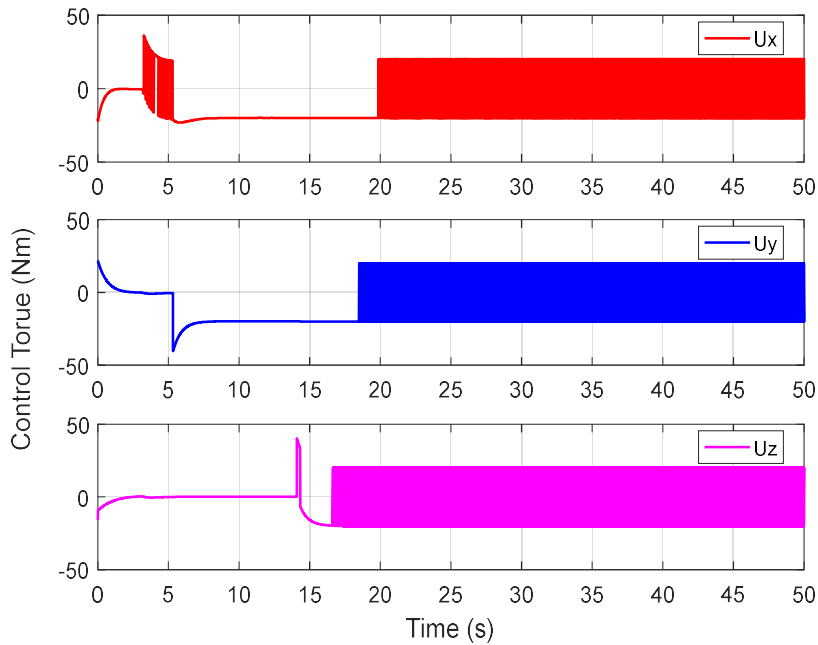


Fig 6.7: Control torque. (Sign)

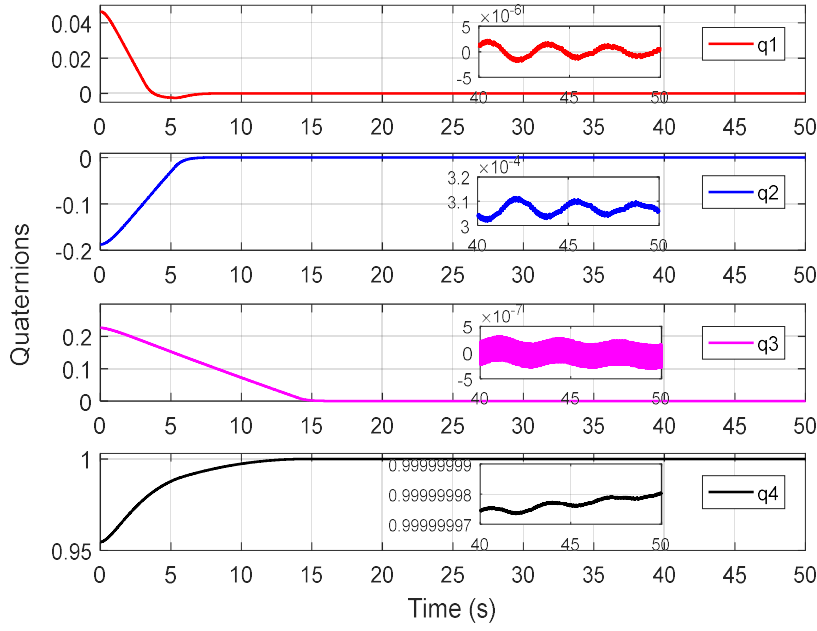


Fig 6.8: Quaternions. (Sign)

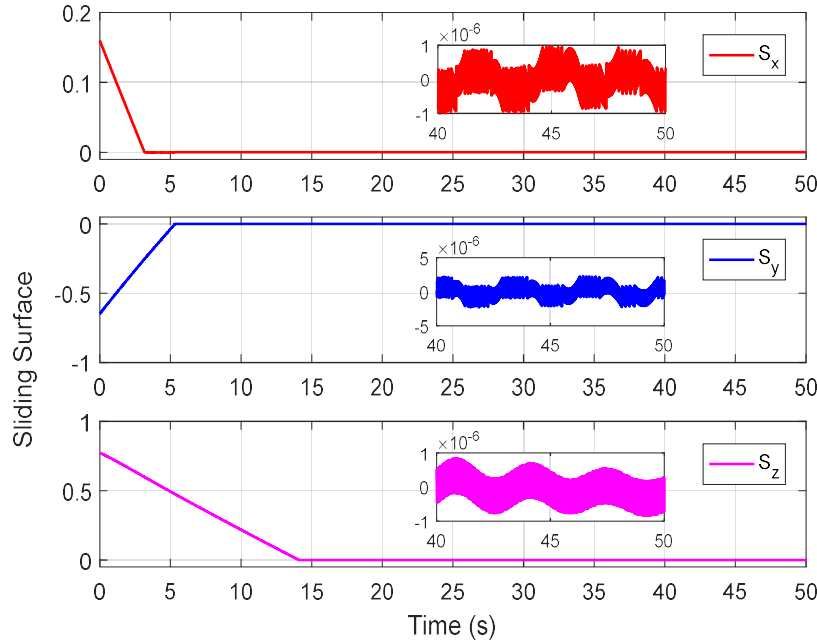


Fig 6.9: Sliding surface. (Sign)

Fig 6.7, Fig 6.8, and Fig 6.9 illustrate the control torque, quaternions, and the sliding surface, respectively. It is observed that the sliding surface converges to zero, but with oscillatory behavior. This oscillation can be attributed to the control torque, which exhibits high and irregular frequency oscillations. This phenomenon is known as chattering, and it poses practical challenges for implementation as it exceeds the actuators' operating limits due to the instantaneous changes in applied torque values. Moreover, the resulting performance is unsatisfactory. Consequently, to enhance the system's response, the sign function will be replaced with alternative functions.

- **Using saturation function**

To overcome the undesirable results obtained using the sign function, an alternative method employing the saturation function is introduced. The optimized parameters of the controller for this approach are shown in Table 6.2.

Table 6.2: Control parameters using saturation function.

Controller part	Control gain	Value
SMC	k	3.835
	K_1	20
	K_2	9.5974

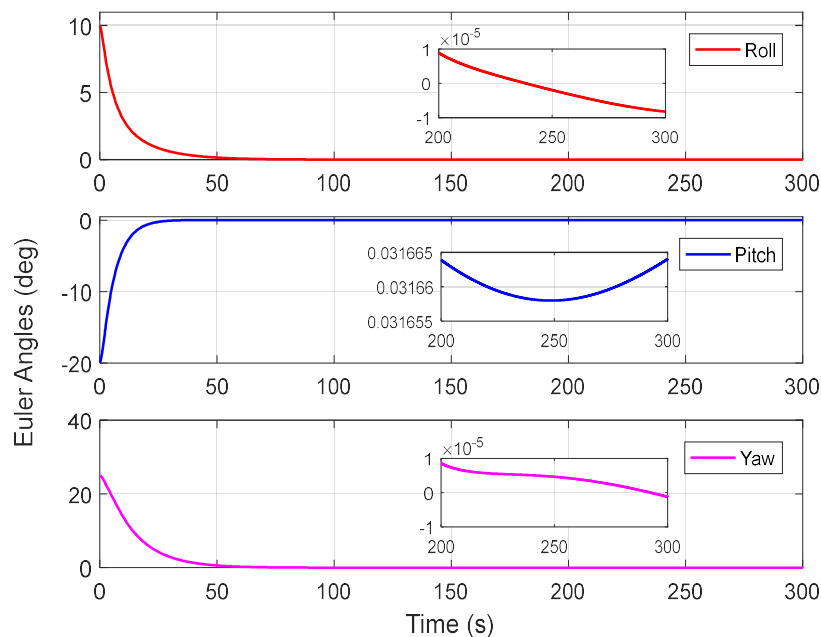


Fig 6.10 : Euler angles. (Sat)

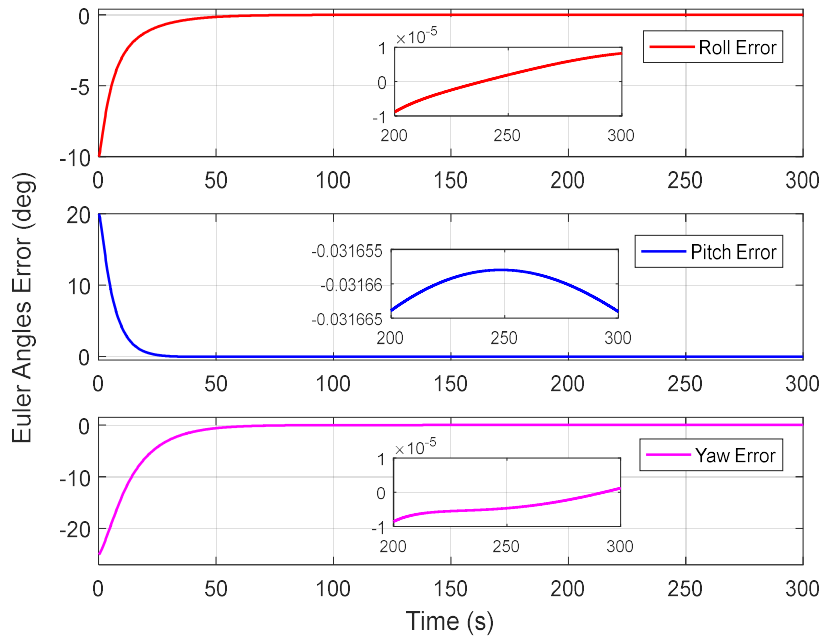


Fig 6.11: Euler angles error (Sat)

Fig 6.10 and Fig 6.11 demonstrate satisfactory results, with the controller effectively enabling the attitude to converge towards the desired state. The angle errors converge smoothly to zero, indicating precise attitude performance. Furthermore, the control torques exhibit reasonable magnitudes and dynamics, ensuring practical feasibility for implementation on real systems. These results validate the effectiveness of the proposed control approach based on the saturation function in reducing the chattering phenomenon while maintaining satisfactory tracking performance.

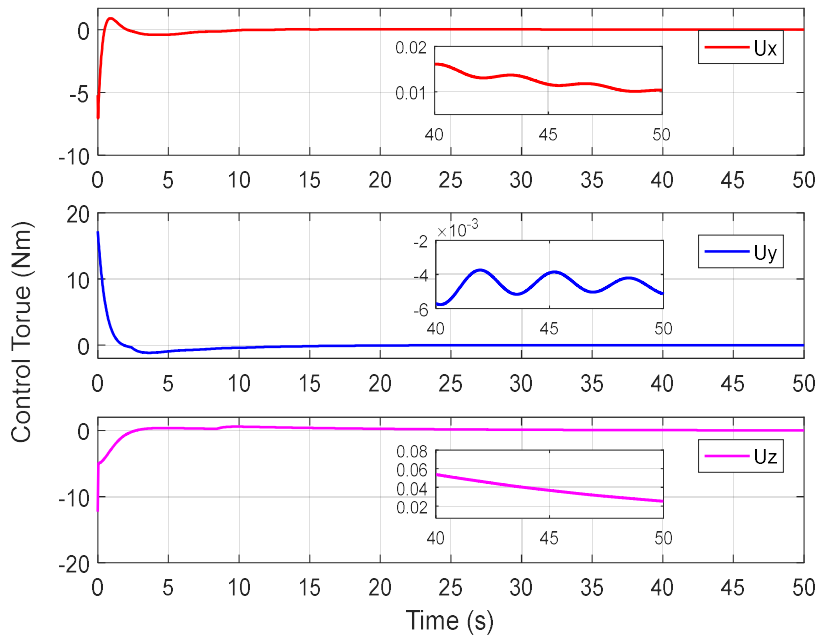


Fig 6.12: Control torque. (Sat)

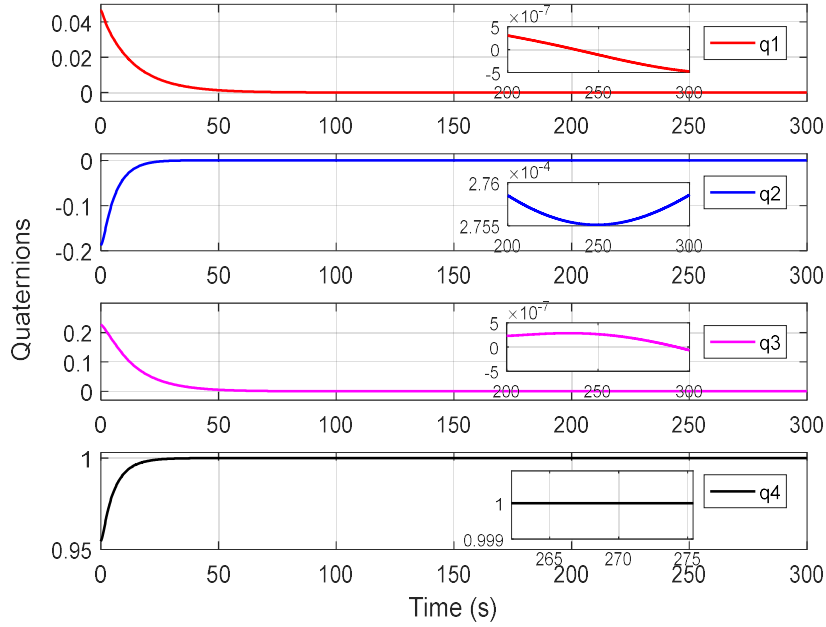


Fig 6.13: Quaternions. (Sat)

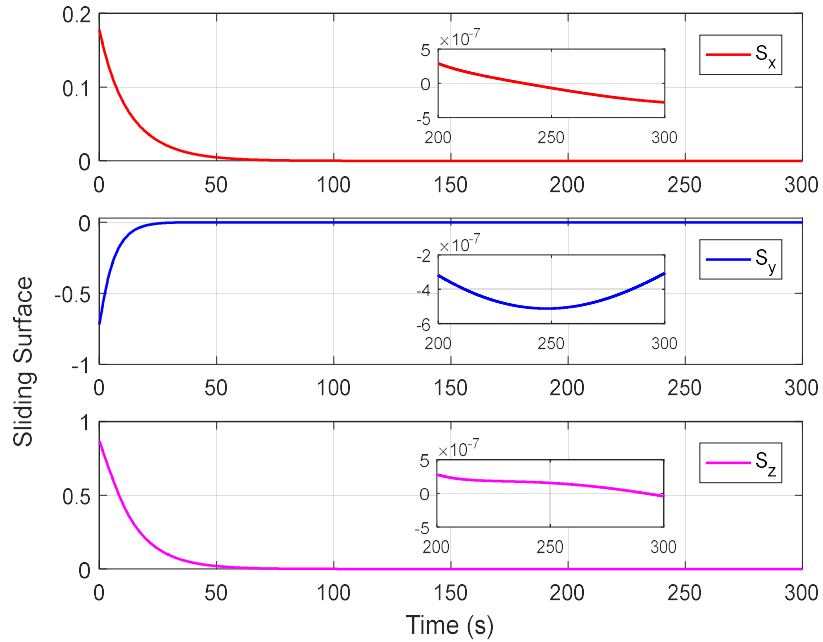


Fig 6.14: Sliding surface. (Sat)

In Fig 6.12, we notice that the chattering is eliminated, and the maximum torque values applied on the x, y, and z axes, respectively, are smaller than the torque produced by the controller using the sign function. Additionally, an improvement in the response is observed in the quaternion and the sliding surface, as shown in Fig 6.13 and Fig 6.14.

- **Using The Hyperbolic tangent function**

By employing the PSO method, the controller parameters were fine-tuned to achieve the desired system performance, with the optimized values as follows:

Table 6.3: Control parameters using hyperbolic tangent function.

Controller part	Control gain	Value
SMC	k	10.0993
	K_1	20
	K_2	16.6154

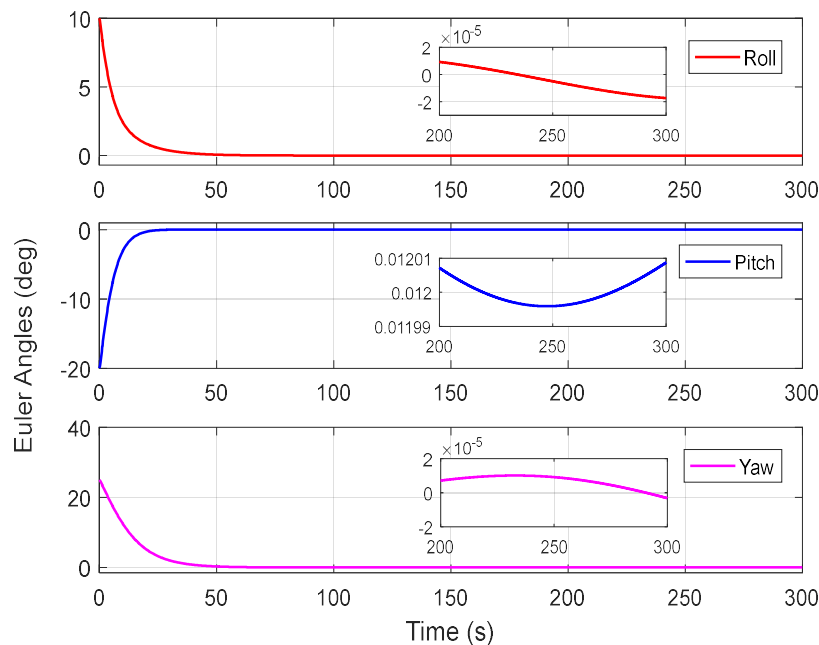


Fig 6.15: Euler angles. (H-tan)

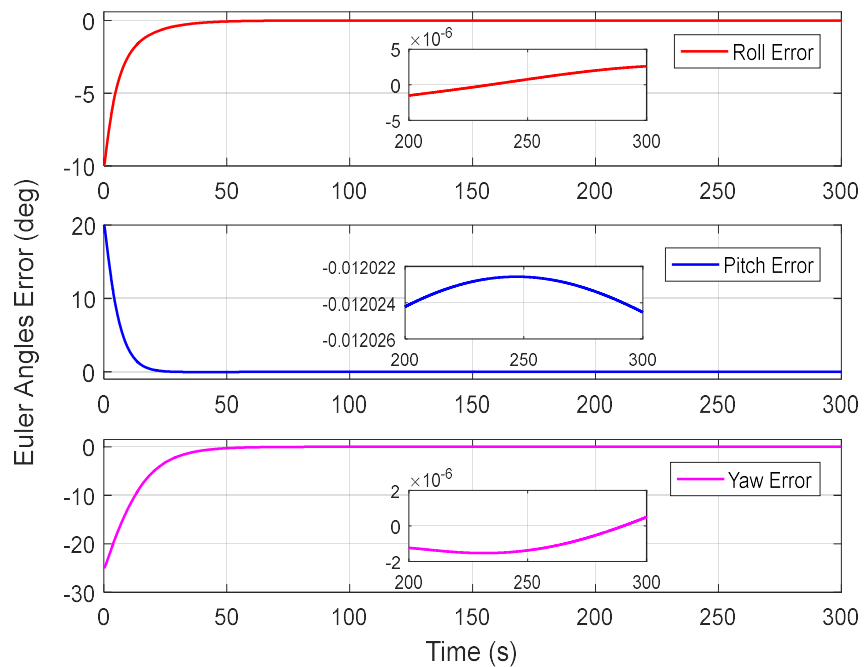


Fig 6.16 : Euler angles error. (H-tan)

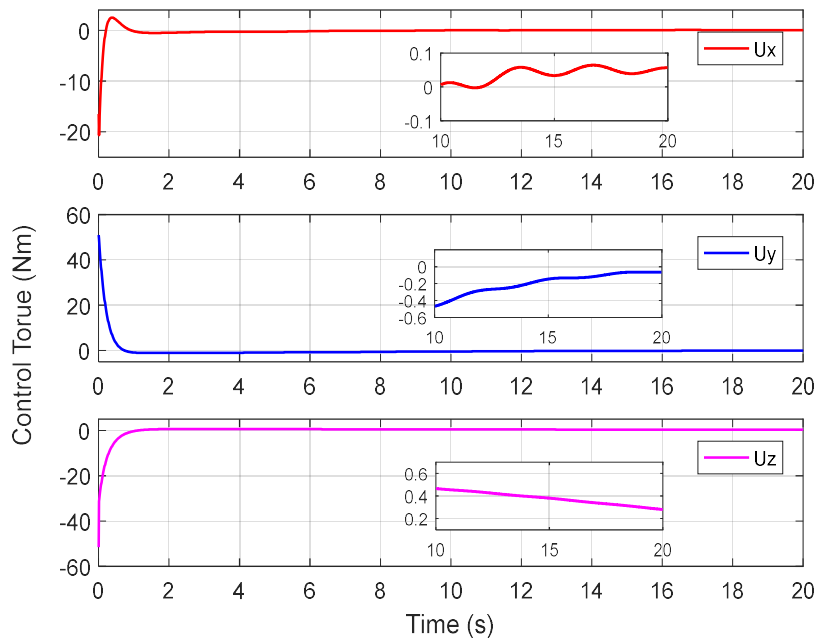


Fig 6.17: Control torque. (H-tan)

As we can see from Fig 6.15 and Fig 6.16, the responses of Euler angles are satisfying. This results from the improvement in the control torque in Fig 6.17.

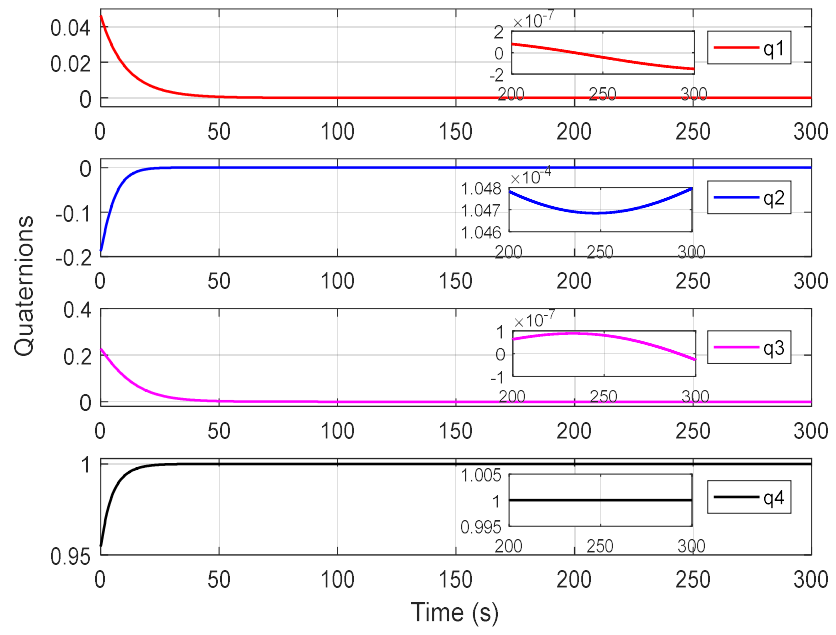


Fig 6.18: Quaternions. (H-tan)

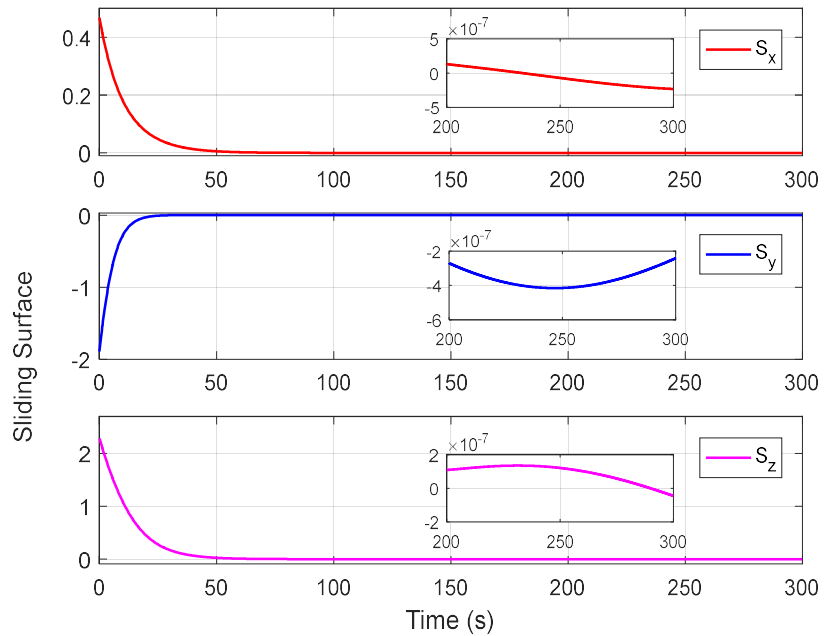


Fig 6.19: Sliding surface. (H-tan)

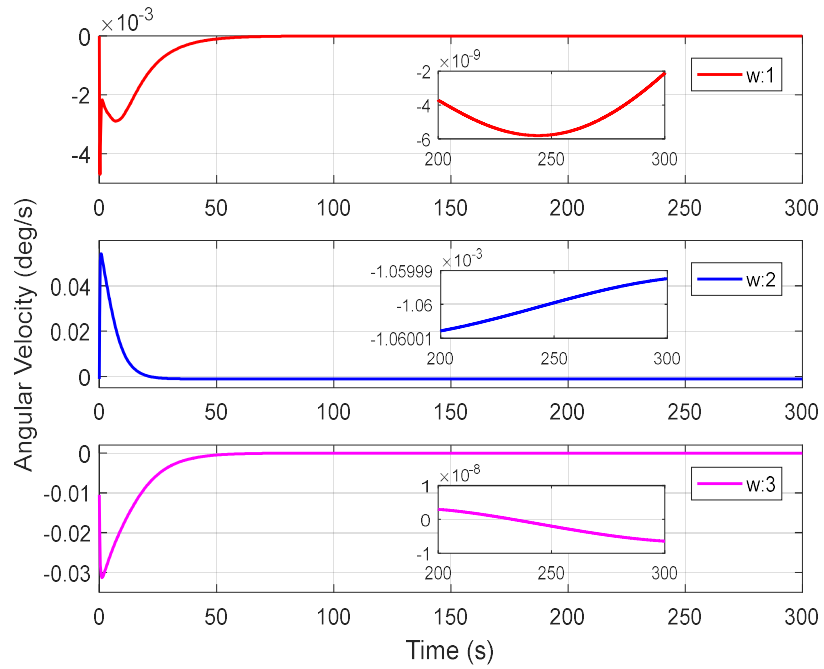


Fig 6.20: Angular velocity. (H-tan)

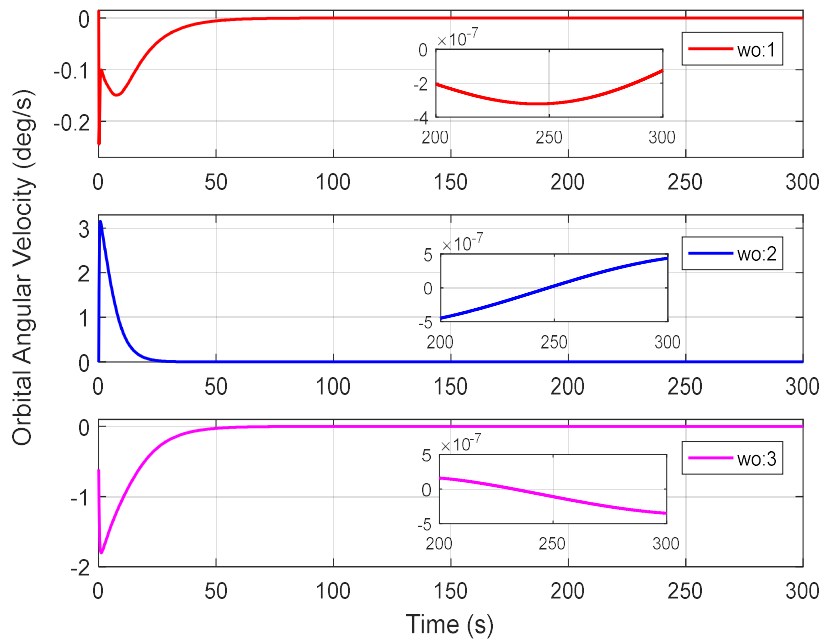


Fig 6.21: Orbital angular velocity. (H-tan)

Fig 6.20 and Fig 6.21 represent the angular rate and orbital angular velocity of the system. The angular velocity and rotational speed initially vary until they stabilize around 0 deg/sec as the attitude trajectory approaches the desired reference.

6.5.2. Adaptive Sliding Mode results

The selection of optimal gain values for the Sliding mode controller is achieved through a systematic process of the 'trial and error' method; by applying this method, we were able to fine-tune the parameters to achieve the desired performance as follows:

Table 6.4: Control parameters using Adaptive sliding mode.

Controller part		Control gain	Value
ASMC	First method	u_m	5
		σ	0.02
		γ	0.002
	Second method	τ	30
		$\bar{\sigma}$	2
		\bar{k}	2
		$\epsilon, \epsilon_0, \epsilon_1, \epsilon_2$	0.1
		p_0, p_1, p_2	1

- **Method 1**

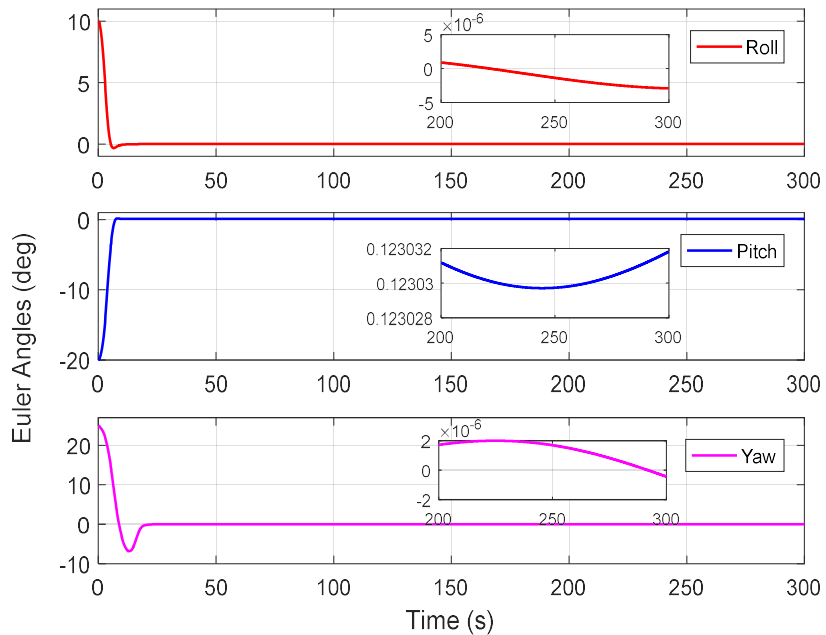


Fig 6.22: Euler angles. (ASM1)

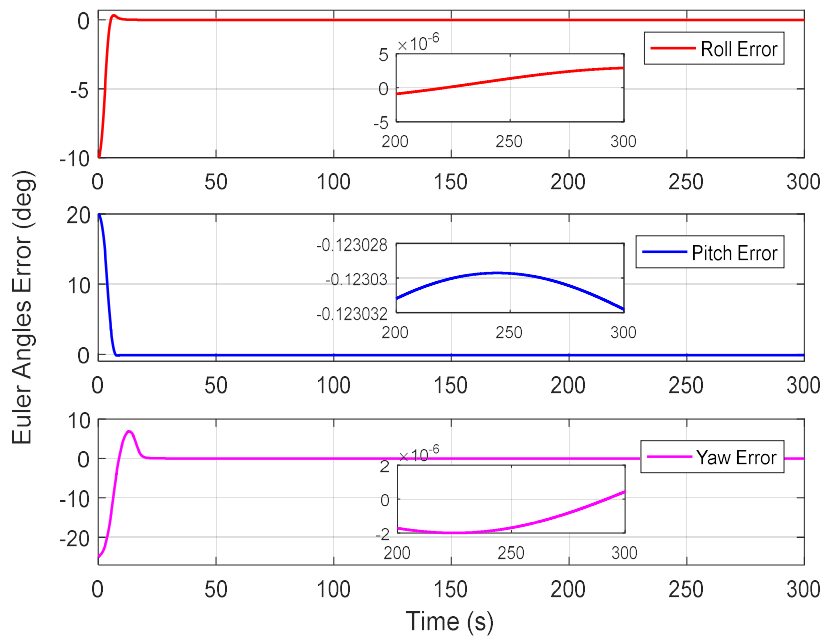


Fig 6.23 : Euler angles error. (ASM1)

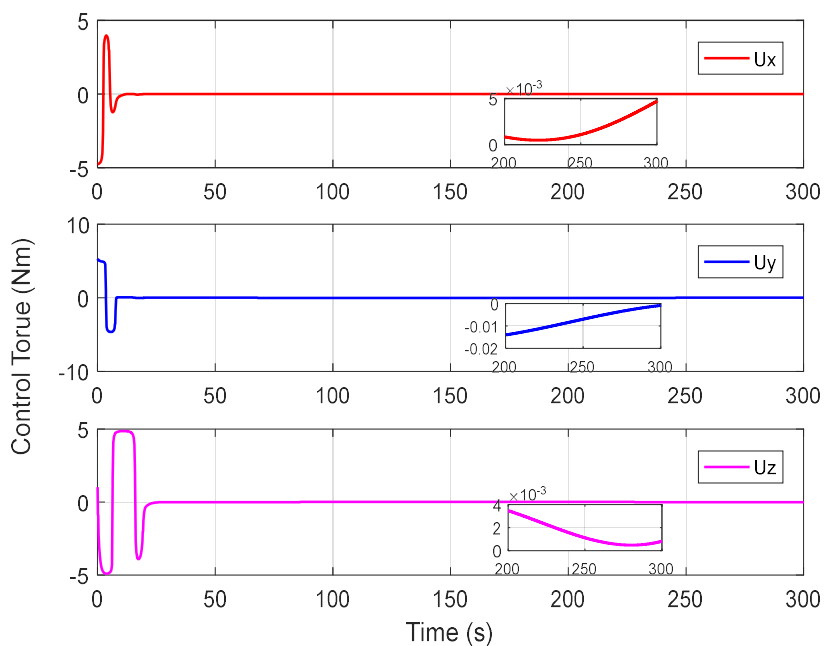


Fig 6.24: Control torque. (ASM1)

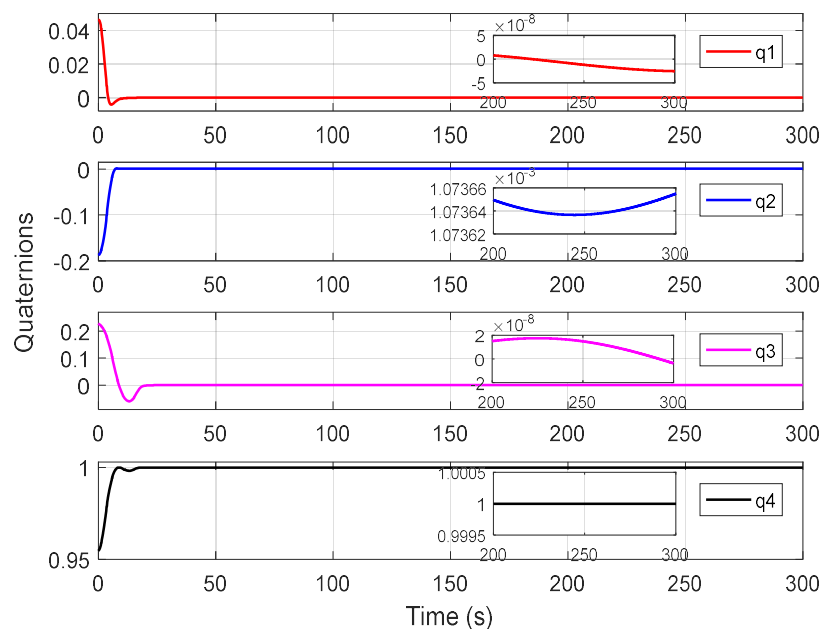


Fig 6.25: Quaternions. (ASM1)

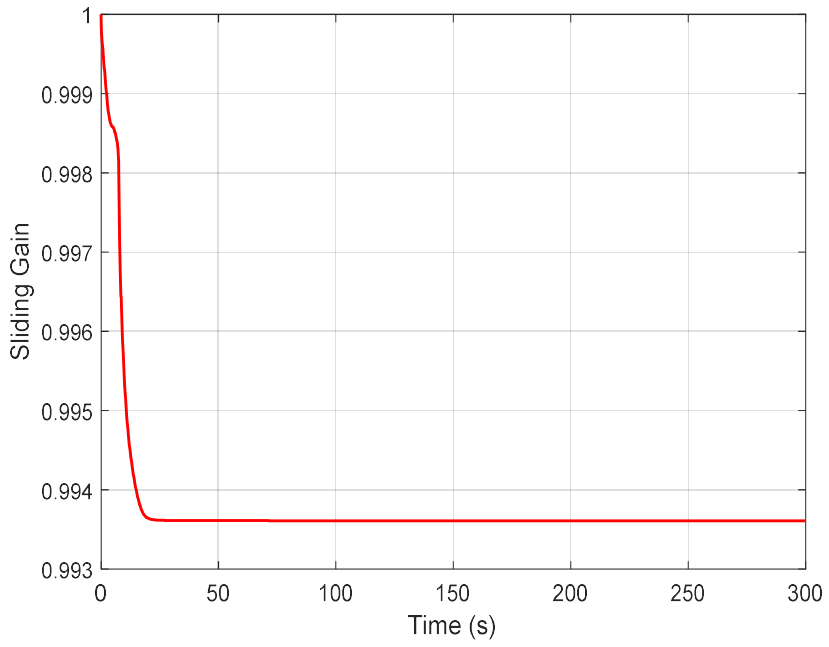


Fig 6.26: Response of $\rho(t)$. (ASM1)

The response of the closed-loop system for method 1 is shown in Fig 6.22-Fig 6.26. It is seen that the control objective is achieved despite the presence of disturbances and the quaternions converge to zero (Fig 6.25). It is also noted that $\rho(t)$ decreases during the transient, but then converge to a constant value ($\rho=0.9935$).

- **Method 2**

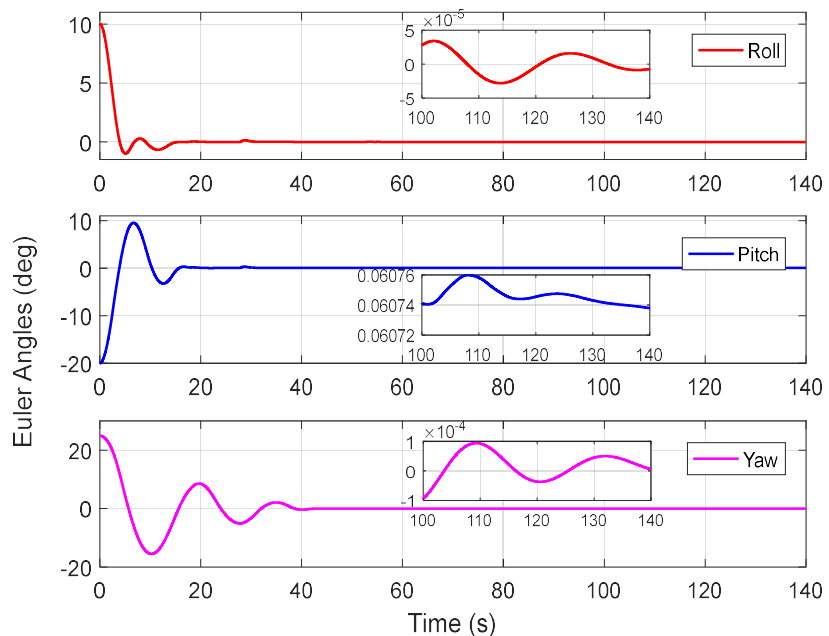


Fig 6.27: Euler angles. (ASM2)

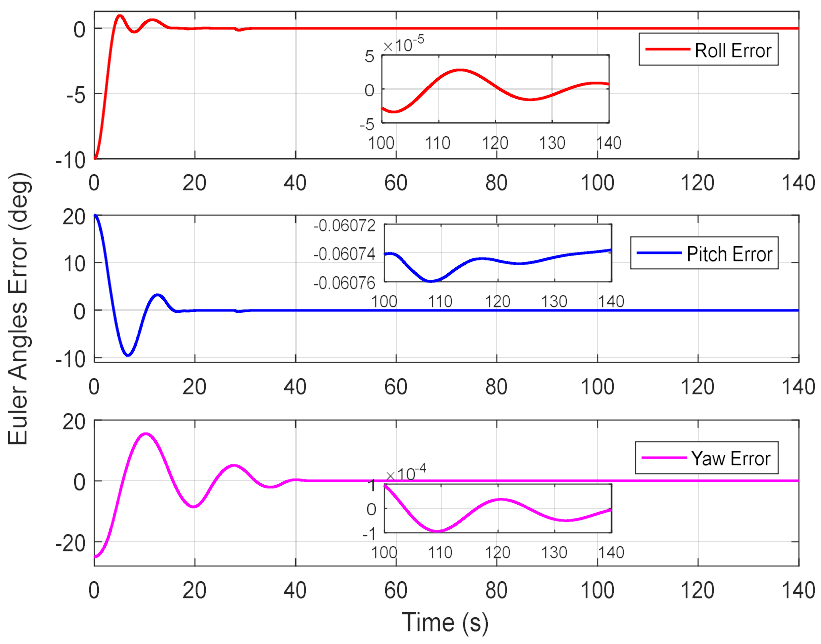


Fig 6.28: Euler angles error. (ASM2)

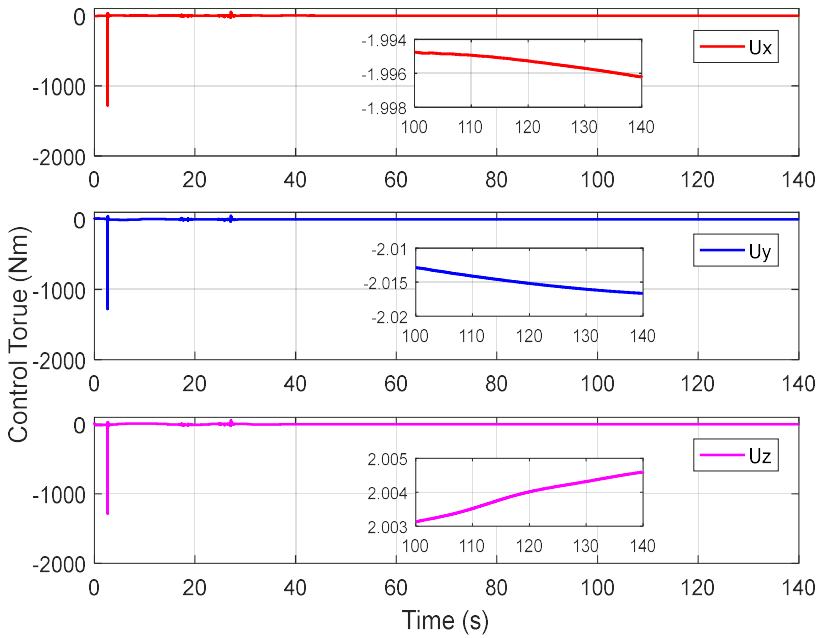


Fig 6.29: Control torque. (AMS2)

Fig 6.29 shows the input control torque. It is clear that the undesired chattering due to its discontinuous when crossing the sliding surface is reduced effectively due to the estimation of the disturbances.

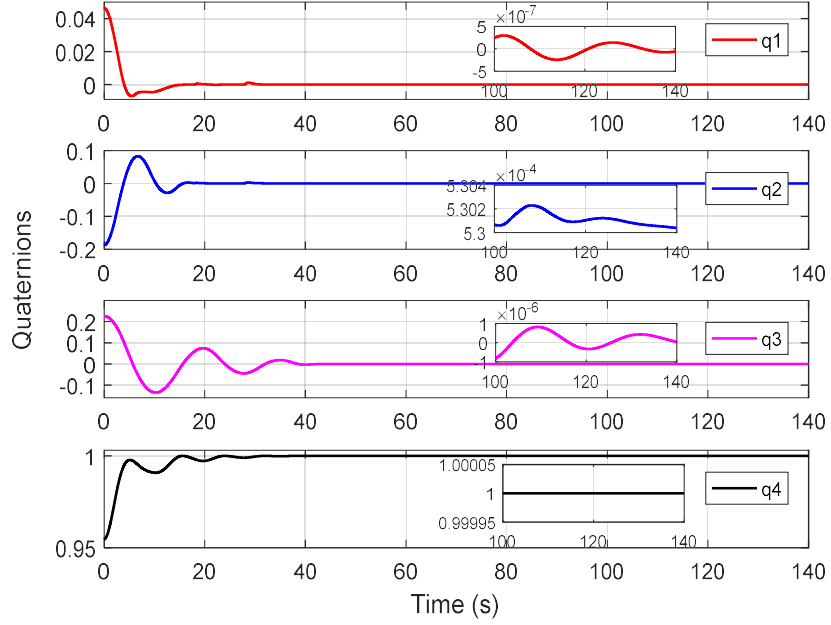


Fig 6.30: Quaternions. (AMS2)

The attitude quaternion, displayed in Fig 6.30, clearly demonstrates that the adaptive sliding mode controller achieves robust performance in attitude stabilization. This effectiveness is further illustrated in Fig 6.27 and Fig 6.28, where the controller's impact on system stability is evident.

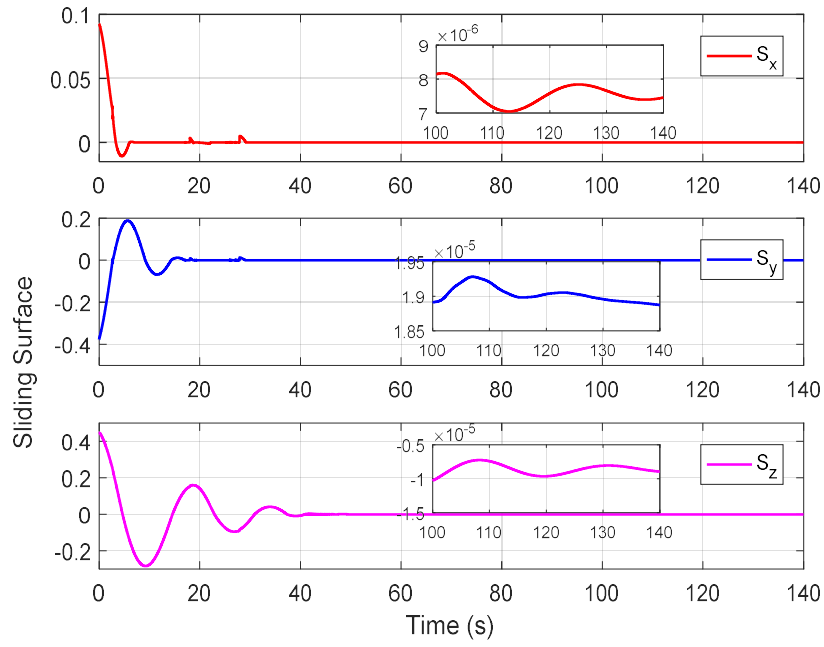


Fig 6.31: Sliding surface. (AMS2)

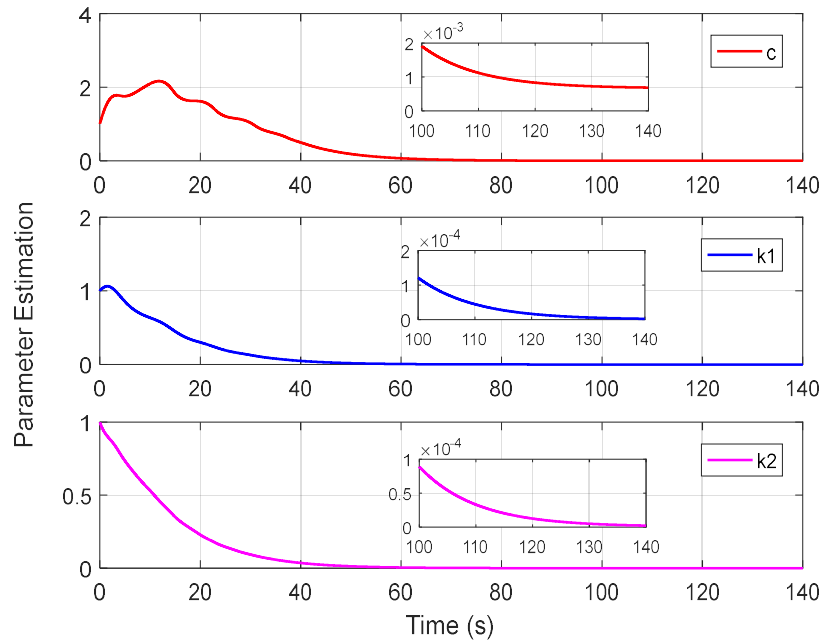


Fig 6.32: Estimated parameters. (AMS2)

The corresponding estimated parameters are shown in Fig 6.32. It is clear that the parameters \hat{c} , \hat{k}_1 and \hat{k}_2 converge to constants with the initial conditions $\hat{c}(0) = 1$, $\hat{k}_1(0) = 1$ and $\hat{k}_2(0) = 1$, respectively.

Table 6.5: Comparison between different controllers.

	SMC			ASMC	
	$\text{sign}(S)$	$\text{sat}(S)$	$\tanh(S)$	Method 1	Method 2
RMSE ϕ (deg)	3.497e-05	8.247e-06	2.616e-06	5.829-07	2.594e-05
RMSE θ (deg)	0.03523	0.03166	0.01202	0.1231	0.06071
RMSE ψ (deg)	2.457e-05	1.215e-06	5.025e-07	3.194e-07	1.628e-05
RMSE (deg)	0.03523	0.03166	0.01202	0.1231	0.06071

Table 6.5 shows that the sliding mode controller utilizing the hyperbolic tangent function achieves faster convergence towards the desired performance. It also exhibits enhanced accuracy across all angles (Roll, Pitch, Yaw), demonstrating superior control characteristics.

6.6. Conclusion

In this chapter, the problem of spacecraft attitude stabilization systems with multiple disturbances is investigated. The focus is primarily on the proposed methods, namely Sliding Mode Control (SMC) and Adaptive Sliding Mode Control (ASMC). These methods are presented and detailed extensively. A disturbance observer is designed to estimate the lumped disturbances. Furthermore, using the estimated information, a robust sliding mode control approach integrated with adaptive parameter laws is designed. The parameters were optimized using Particle Swarm Optimization (PSO) to ensure that the control systems achieve optimal performance. Finally, the convergence and stability of the closed-loop system are analyzed. The simulation results demonstrate that the proposed method performs well and can effectively accommodate disturbances in the flexible spacecraft control system. Our future work will focus on designing the controller using output information rather than state variables. Considering the importance of security and tracking control in spacecraft systems, our future research will also extend to fault detection